# UC San Diego
## UC San Diego Electronic Theses and Dissertations

**Title**

3D Printing of Microstructures for Cellular Investigation and Biomimicry

**Permalink**

https://escholarship.org/uc/item/9g7465xq

**Author**

Meggs, Kyle

**Publication Date**

2015

Peer reviewed|Thesis/dissertation

UNIVERSITY OF CALIFORNIA, SAN DIEGO

3D Printing of Microstructures for Cellular Investigation and Biomimicry

A Thesis submitted in partial satisfaction of the requirements
for the degree Master of Science

in

Nanoengineering

by

Kyle Meggs

Committee Members:

Professor Shaochen Chen, Chair
Professor Michael Heller
Professor Donald Sirbuly

2015

The Thesis of Kyle Meggs is approved, and it is acceptable in
quality and form for publication on microfilm and electronically:

_____

_____

_____

Chair

University of California, San Diego

2015

Dedication

I would like to dedicate this work to my mother

Table of Contents

List of Figures

ABSTRACT OF THE THESIS


3D Printing of Microstructures for Cellular Investigation and Biomimicry


by


Kyle Meggs


Master of Science in Nanoengineering


University of California, San Diego, 2015


Professor Shaochen Chen, Chair


Herein we describe methods of light-based printing for cellular applications and biomimicry. Light based printing offers a non-contact form of printing which can reach resolutions below 100nm. Here we describe both additive and subtractive manufacturing,

demonstrating the remarkable flexibility of light based printing techniques. Two different

fabrication systems are employed for this 3D printing. The first is a femtosecond laser,

capable of printing resolutions below 100nm via photopolymerization. This same laser

was also used for ultrafast laser induced degradation (ULID) of gold nanorod-collagen

composites. The second fabrication system utilized is a digital micro-mirror device

(DMD) which utilizes over a million micro-mirrors for rapid projection printing with

resolution down to a few microns. Combining these two unique systems allows for

creative and novel manufacturing on a large scale with the DMD, but with fine resolution

from the femtosecond laser. In the first project presented, 3D web-like structures were

fabricated as cell scaffolds to study cellular interactions with never before studied

mechanical tuning of Poisson' ratio. In the second project presented, nanorod laden

collagen was degraded via ULID to create 3D channels in collagen with encapsulated

cells. Finally, in the last project presented, biomimetic structures were created with the

femtosecond laser to replicate natural trichomes which are used to entrap the common

bed bug.

# **Chapter One:** Introduction

The bulk of my research relied on the use of light to create 3D microstructures. Recently, large scale 3D printing techniques have revolutionized prototyping and custom printing for a multitude of different industries. Traditional methods of 3D printing such as extrusion printing rely on additive techniques through material deposition which do not easily scale down to the micron range. Light based techniques are photon based and thus inherently microscopic, but can also readily be scaled up to create larger structures. This research will detail how two devices, a femtosecond laser and a digital micromirror device (DMD) can offer the sort of flexibility of traditional 3D printing, but on the micron scale. Chapter Two will describe the systems used for fabrication in detail. Chapter Three will describe how the femtosecond laser can employ two-photon polymerization to create web-like scaffolds with tunable geometric and mechanical properties, and how those properties were tuned to investigate the scaffolds' Poisson's ratio. Chapter 4 will describe ultrafast laser-induced degradation (ULID) of hydrogels through gold nanorod absorption of near infrared light to form channels in gels with encapsulated cells. Chapter Five will describe how the femtosecond laser can also create structure which can interact with entire organisms. In this final chapter we fabricated trichomes, or hooks, which are based the naturally occurring trichomes present on the surfaces of bean leaves and which have been used to eradicate bed bugs

   All of these applications of light based 3D printing share one thing: inspiration from nature, or biomimicry. The scaffold structures were designed with a negative Poisson's ratio so that when they are stretched in one direction, they expand in the other direction. This is unlike almost all other man made materials which have a positive Poisson's ratio. These materials, which have a negative Poisson's ratio are called 'auxetics' and behave like some types of skin tissues and soft tissues. The channels formed by ULID are based on the branch-like layout of naturally occurring blood vessels. By creating structures which cells can conform to and reinforce, we can create platforms for advanced tissue engineering applications. The trichomes are obviously based on the naturally occurring hooks from bean leaves. The design of the structures is similar to the naturally occurring trichomes but rational design can allow for increased potency through design adjustments.

# **Chapter Two:** Fabrication Systems

## 2.1 Femtosecond Laser System

### *2.1.1 Introduction*

All of the research presented in this thesis was dependent on the unique features of the femtosecond laser system (Vitesse, Coherent Inc. Santa Clara, CA) with the following parameters: wavelength ($\lambda$) = 800nm; repetition rate = 80 MHz; pulse duration = 100 femtoseconds. The two features of the femtosecond laser which allowed it to play such an integral part to this research are the ultrashort pulse on the femtosecond scale and the 800nm wavelength light. The significance of the ultrashort pulse is the increased peak power provided by the femtosecond laser, much higher than that of continuous wave laser. This can be exploited through two-photon polymerization (TPP) whereby a liquid or gel-like polymer undergoes TPP and crosslinks to become solid. The other feature which makes femtosecond lasers particular useful in biological applications is the wavelength. The femtosecond laser used in this research operates at 800nm in the infrared range. This allows for optical penetration through biological samples due to limited absorption of 800nm light.

The laser itself is stationary and samples for laser irradiation were placed on an automated three-dimensional scanning stage. Complex patterns such as those in Figure 2.1 were written in G-code (a numerical control programming language for computer-aided manufacturing) and read through the MS-2000 stage and loaded to a Tracer®

program which was also developed by the stage manufacturing. We used a shutter to control laser exposure and the Tracer® program controlled both the movement and shutter simultaneously. G-code was written in both absolute and relative coordinates determined by design of structure. Python was used to make iterations of code for larger structures. Figure 2.2 shows a complex structures fabricated in layer by fabricating a single layer then changing the Z, or laser focal plane, and creating a new, identical layer.

*2.1.2 Mechanism of Two-Photon Polymerization in 3D*

Two-Photon polymerization (TPP) is made possible through the mechanism of two-photon absorption (TPA). TPA was first predicted in 1931 by physicist and Nobel laureate Maria Goeppert Mayer in her doctoral thesis which was defended in front of three future Nobel laureates: Max Born, James Franck and Adolf Otto Reinhold Windaus. TPA is the process whereby one molecule is excited to a higher energy state by absorbing two photons simultaneously. The energy of the excited state is equal to the sum of the energy of the two photons. The process is a nonlinear optical process as it depends on the square of the light intensity. While first predicted in 1931, TPA was not observed until after the invention of the laser and, following the invention of the ultrafast femtosecond laser in the 1980's, finally used to create structures via two-photon polymerization.[1]

Photopolymerization is the process where a polymer or monomer forms long polymer chains due to exposure to light. The photopolymerization in this research was observed by the change from liquid polymers to solid polymers for 3D fabrication. Essentially, the material for fabrication was placed in liquid form in the path of the light

and then certain parts were selectively exposed in order to polymerize or induce a phase change to 'harden' them into a solid. Photoinitiator was added to monomers so that when the photoinitiator-monomer solution was exposed to light of a wavelength matching that of the photoinitiator, it could provide free radicals for the polymerization process. Upon exposure to light, the photoinitiator simultaneously absorbs two photons and produces a free radical. The free radical then attacks the C=C bonds of the monomers to produce monomers with free electrons. Then the monomers with free electrons attack other monomers to form oligomers with free electrons. This process continues until two radicals neutralize each other.[2]

The femtosecond laser is only able to take advantage of TPP due to the extremely high photon density at the center of the laser voxel. A voxel is a three dimensional pixel and is a portmanteau for the words 'volume' and 'pixel'. In this case the laser voxel is the laser spot which is described as a 3D, spherical spot, and is slightly elongated in the Z direction (Figure 2.3). The elongation in the Z direction can be problematic when trying to create extremely small structures so using a high stage speed, low power and focusing the focal point such that the entire voxel is not exposed to the polymer can restrict the Z dimension and increase the resolution. The high density of the laser spot central TPP volume is advantageous because the cross section for two photon absorption is much smaller than that of one photon absorption, or the entire beam (Figure 2.3B). The Gaussian distribution of the laser beam means the outer part of the spot, or fringe of the beam does not contain high enough power to achieve TPP and therefore does not polymerize the structure. The limitation allows for extremely small structure creation

with sub-100 nm spatial resolution, smaller than the diffraction limit, thus offering an advantage over one photon polymerization (OPP).[2]

In order for TPP, a photoinitiator must be added to the monomer or polymer. Then the following three conditions can be met. (1) Both the photoinitiator and monomer material need to be transparent at the laser wavelength (800nm in this case) to allow for 3D focusing. (2) The monomer needs to also be transparent at the two photon absorption wavelength ($\lambda/2 = 400$nm) to avoid thermal damage. (3) The photoinitiator must absorb at the two photon wavelength and have highly active radical species generation.[1] Because the polymers used for fabrication (and water) have very low absorption of NIR light, the laser is able to crosslink deep in the polymer without having an effect on the polymer (or cells) between the focal point and the laser. In summary, neither the photoinitiator nor the monomer/polymer solutions absorb the wavelength of the laser (800nm). However, at the TPP volume at the center of the laser spot, material is able to absorb two photons simultaneously, effectively absorbing 400nm light. By using photoinitiator which provides free radicals only on exposure to 400nm light, we can activate photopolymerization *only* at the TPP volume.

*2.1.3 Mechanism of Gold Nanorod Absorption for Collagen Degradation*

The research presented in Chapter Five is based on heat degradation via gold nanorod absorption of NIR light. In this case, TPP was not utilized or useful. The gold nanorods used were synthesized such that their longitudinal surface plasmon peak coincided with the laser wavelength of 800nm. Gold nanorod absorption at their plasmon

resonance produces a photothermal effect due to excited electrons on the surface releasing energy in the form of phonons. Localized Surface Plasmon Resonance (LSPR) is the resonant oscillation of conduction electrons due to incident light on a conductive nanoparticle smaller than the incident wavelength.[3] As the size of gold nanorods decreases below the wavelength of light and while there exists a difference between the longitudinal (long) and transverse (short) axis, gold nanorods exhibit two plasmon absorption bands, one corresponding the length of the transverse axis and one to the length of the longitudinal axis.[4] The longitudinal (longer) peak corresponds to the longer wavelength of light (800nm) and the transverse (shorter) peak corresponds to the shorter wavelength of light (520nm) and represent the same peak as the plasmon band of spherical particles. Essentially, one can tune the size of gold nanoparticles to match a certain wavelength of light. Then, at this wavelength, the gold nanorods will strongly absorb the light and convert it into heat. Because the nanorods are not spherical there is a long length and a short length which each correspond to different wavelength of light. The transverse peak largely remains constant but the longitudinal peak red shifts as the aspect ratio increases.[5] The aspect ratio is defined as the length of the longitudinal axis divided by the length of the transverse axis. For this reasons the longitudinal axis is the one tuned to absorb the wavelength of lights. Absorption of light at the plasmon resonances produces a photothermal effect due to exited electrons on the surface releasing energy in the form of phonons which act as physical heat carriers. Phonons are collective oscillations of atoms and at long-wavelengths carry sound, and in this case, at short wavelengths, carry heat.[6] This heat is then released into the environment and rapidly heats the surrounding collagen gel, causing it to liquefy and produce a hollow

channel. It is these channels which cells migrate to and reinforce to form blood vessel-like structures.

## 2.2 DMD

In addition to using the femtosecond laser for fabrication, our lab also employs digital micromirror devices (DMD) to rapidly produce larger structures by layer-by-layer projection printing. A UV light is shone on the DMD which then reflects the light to the photopolymer to polymerize it. A DMD is simply an array of hundreds of thousands to over a million aluminum micromirrors which are either in an on or an off position. An on position (mirror at a +10 degree angle) means the mirror reflects the light to the sample, while an off position (mirror at a -10 degree angle) means the mirror reflects the UV light to the light absorber. This results in 'on' mirrors sending a beam of light to the sample, and 'off' mirrors not sending a beam of light (Figure 2.4). Using computer aided design (CAD), one can design complex shapes, pixel by pixel, mirror by mirror, and print layer by layer 3D structures by polymerizing, or hardening the photopolymer when the mirrors are 'on' and leaving the spots untouched by UV light as liquid, where the mirrors are 'off'. The polymerization mechanism is very similar to that described above regarding the femtosecond laser. The DMD devices do not take advantage of two-photon polymerization and are thus restricted to larger, or worse resolution. Prior to fabrication, photoinitiator is added to the solution to provide free radicals as described earlier in this chapter. The wavelength of the UV light is similar to the wavelength where the laser achieves for TPP (400nm) so often the same material and photoinitiator can be used for convenience.
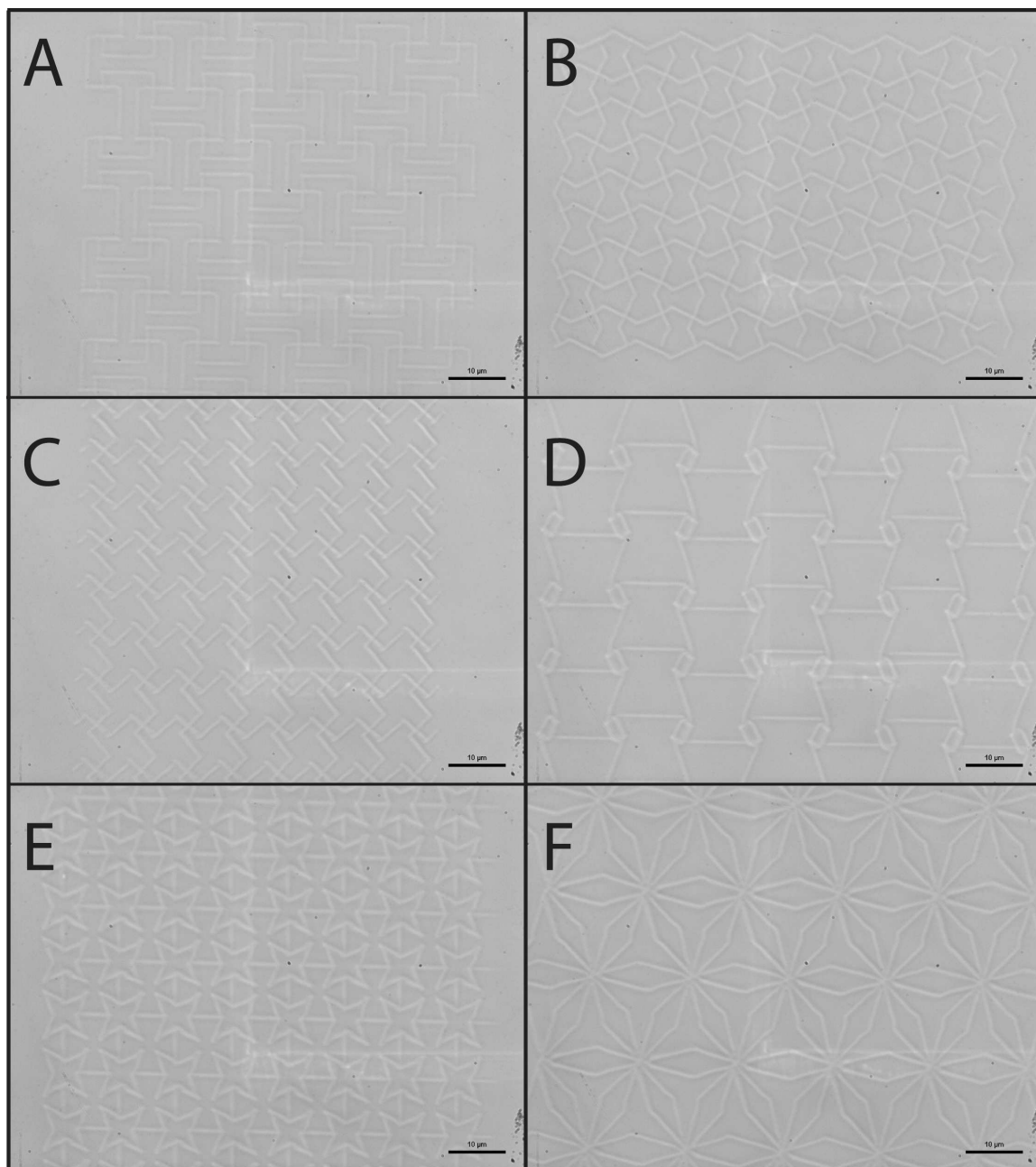
Figure 2.1. This figure shows bright field images of different complex structures fabricated using the laser system. The structures were named 'Grid', 'Hourglass', 'NinjaStar', 'SquareChiral', 'Star', and 'TriStar', from A-F respectively. Scale bar is 10 microns.
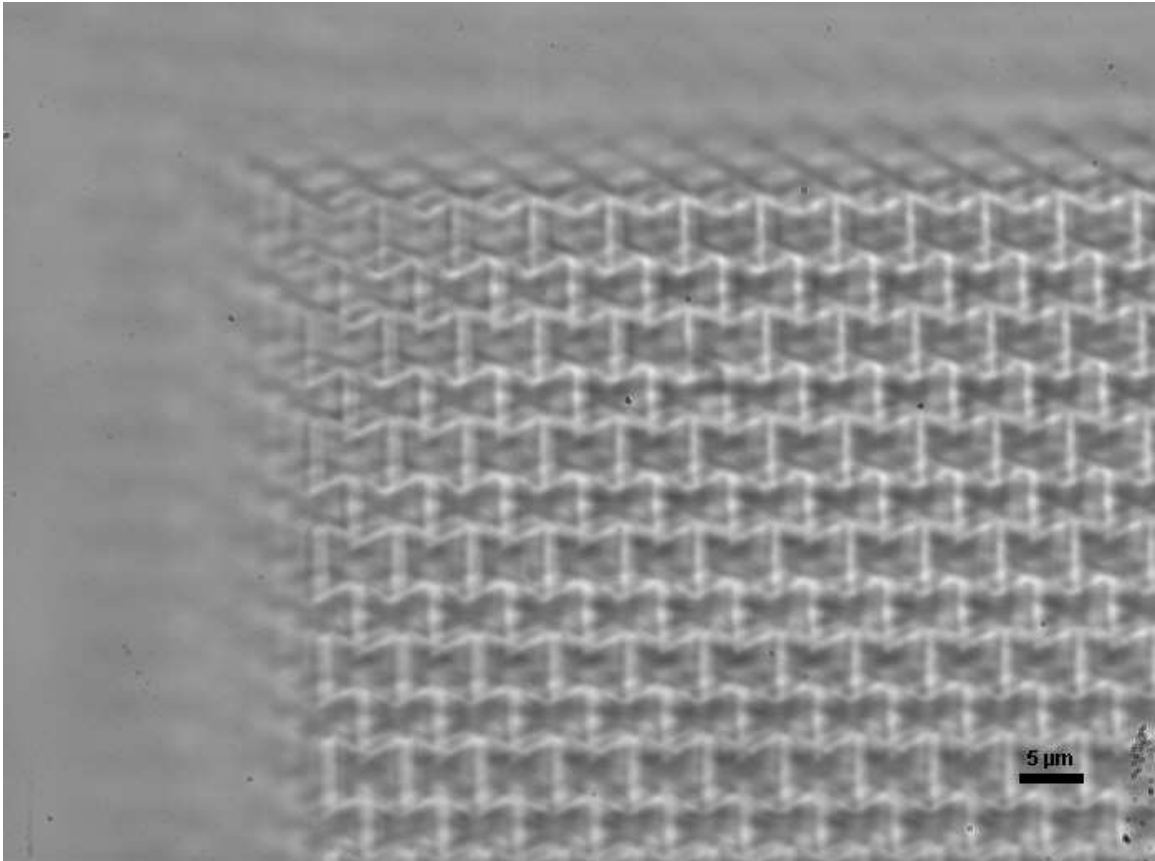
Figure 2.2. This figure shows bright field image of a 10 layer structure of 'Bowtie' structures. Each layer was fabricated in its entirety before the stage was moved 2 microns in the Z direction to change the focal plane. The total height of this structure is 20 microns.
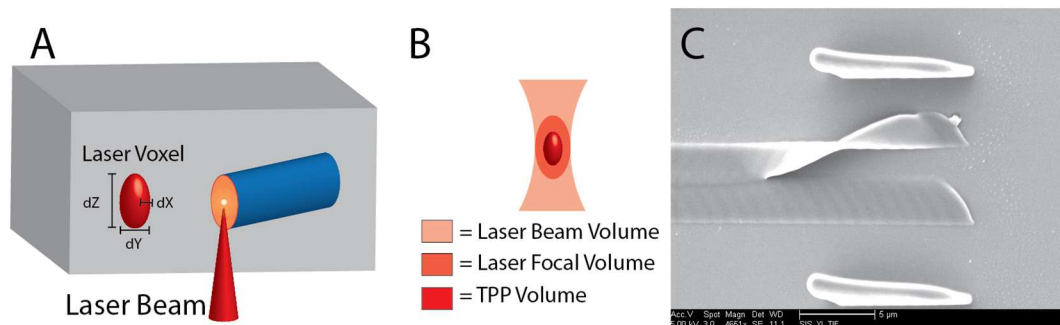
Figure 2.3. Schematic of femtosecond laser voxel in 3D. Figure 2.1A shows the laser beam photopolymerizing the blue structure seen on the right. The left shows a schematic of the laser voxel, displaying the uneven distribution in the Z direction. Figure 2.1B is an SEM picture which shows how a high power leads to an undesirable aspect ratio with a very large dZ. Structures here are upright and some have fallen over. In order to create structures without a poor aspect ratio, higher speeds and lower power must be used. Additionally, focusing the focal point at the glass surface means the bottom of the voxel is cut off from being exposed to the polymer.
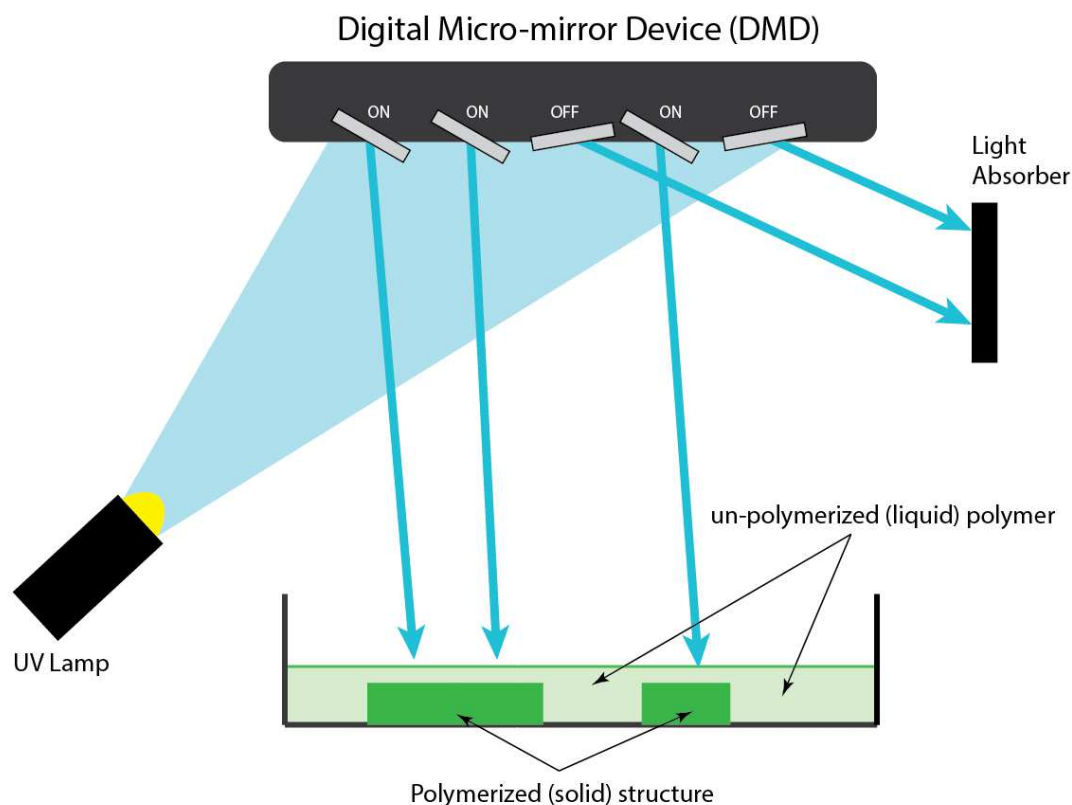
Figure 2.4. Schematic of Digital Micro-mirror Device (DMD). UV light is emitted from the UV lamp towards the DMD. Individual mirror are tilted to an 'ON' or an 'OFF' position. 'On' mirrors send the light to polymerize the sample, while 'OFF' mirrors reflect the light towards a light absorber. A DMD consists of hundreds of thousands of micromirrors which can individually be controlled. Complex shapes can be created by using computer aided design to create layer by layer structures. Once a layer is complete, the stage which holds the liquid polymer can be moved away from the DMD and the fabrication can commence in 3D.

## 2.3 References

1. Malinauskas, M., Farsari, M., Piskarskas, A., & Juodkazis, S. (2013). Ultrafast laser nanostructuring of photopolymers: A decade of advances. *Physics Reports*, *533*(1), 1–31. http://doi.org/10.1016/j.physrep.2013.07.005

2. Fischer, J., & Wegener, M. (2013). Three-dimensional optical laser lithography beyond the diffraction limit. *Laser & Photonics Reviews*, *7*(1), 22–44. http://doi.org/10.1002/lpor.201100046

3. Petryayeva, E., & Krull, U. J. (2011). Localized surface plasmon resonance: nanostructures, bioassays and biosensing--a review. *Analytica Chimica Acta*, *706*(1), 8–24. http://doi.org/10.1016/j.aca.2011.08.020

4. Hribar, K. C., Choi, Y. S., Ondeck, M., Engler, A. J., & Chen, S. (2014). Digital Plasmonic Patterning for Localized Tuning of Hydrogel Stiffness. *Advanced Functional Materials*, *24*(31), 4922–4926. http://doi.org/10.1002/adfm.201400274

5. Link, S., & El-Sayed, M. A. (1999). Spectral Properties and Relaxation Dynamics of Surface Plasmon Electronic Oscillations in Gold and Silver Nanodots and Nanorods. *The Journal of Physical Chemistry B*, *103*(40), 8410–8426. http://doi.org/10.1021/jp9917648

6. Link, S., & El-Sayed, M.A. (2000). Shape and Size Dependence of Radiative, Non-Radiative and Photothermal Properties of Gold NanoCrystals. *Int. Review in Physical Chemistry,* Vol 19, No. 3,409-453. Retrieved from http://www.tandfonline.com/doi/abs/10.1080/01442350050034180#.VVwsgPlVhuA

# Chapter Three: Tuning the Poisson's Ratio of Biomaterials for Investigating Cellular Response

## 3.1 Abstract

Cells sense and respond to mechanical forces, regardless of whether the source is from a normal tissue matrix, an adjacent cell or a synthetic substrate. In recent years, cell response to surface rigidity has been extensively studied by modulating the elastic modulus of poly(ethylene glycol) (PEG)-based hydrogels. In the context of biomaterials, Poisson's ratio, another fundamental material property parameter has not been explored, primarily because of challenges involved in tuning the Poisson's ratio in biological scaffolds. Two-photon polymerization is used to fabricate suspended web structures that exhibit positive and negative Poisson's ratio (NPR), based on analytical models. NPR webs demonstrate biaxial expansion/compression behavior, as one or multiple cells apply local forces and move the structures. Unusual cell division on NPR structures is also demonstrated. This methodology can be used to tune the Poisson's ratio of several photocurable biomaterials and could have potential implications in the field of mechanobiology.

## 3.2 Introduction

Natural tissues and their cellular microenvironment have complex structural and biological heterogeneity and are constantly exposed to a myriad of forces. Materials

scientists have investigated structure–function relationships of cell–materials interactions using various approaches. Cells generate contractile forces on their underlying substrate.[1,2] Over the years, researchers have altered the elastic modulus or stiffness of the substrate by modulating properties such as cross-link density.[3] Alterations in elastic modulus impact a variety of cell types in fundamentally different ways, including motility, gene expression, proliferation, and fate after differentiation.[4–10] These studies have increased our understanding of how cells experience forces, and provided insight into their biophysical mechanisms. However, another fundamental aspect of material properties, the Poisson's ratio, has been largely ignored.

The ability of a biomaterial scaffold to support and transmit cell and tissue forces can be quantitatively described by its elastic modulus and Poisson's ratio. Elastic modulus quantifies a scaffold's elastic behavior in the loading direction, while Poisson's ratio describes the degree to which the scaffold contracts or expands in the transverse direction, perpendicular to the loading direction (Figure 3.1A). Typically Poisson's ratio is assumed to be positive for all materials ($\approx$0.3 to 0.5), even though materials with negative as well as zero values exist in nature. Positive Poisson's ratio (PPR) materials contract transversally when stretched, while a negative Poisson's ratio (NPR) material expands in both the axial and transverse directions. In nature, we come across several materials with a NPR or "auxetics", Examples include crystalline materials,[11–16] carbon allotropes,[17] foams,[18–20] polymers and laminates,[21–24] and other extreme states of matter.[25–28] For naturally occurring materials, the NPR property seems to be an intrinsic property of the material and cannot be tuned according to specific applications. Tuning the Poisson's ratio requires control over the pore interconnectivity and internal

architecture of a material, which can be quite difficult to manipulate. Man-made auxetics have been developed by incorporating rib-containing pores, which modify the shape and deformation mechanisms of polymers, transforming their mechanical behavior to exhibit NPR property.[18,20,22,29–33] These polymers demonstrate well-defined NPR behavior,[18,27,34,35] however, their strain-dependent response is process dependent. For example, polyurethane foams annealed in a compressed state naturally reorganize their cellular microstructure and exhibit NPR behavior.[18,29] However, processes such as annealing offer poor control over the reorganization of cellular microstructure comprising the foams, making it difficult to tune the Poisson's ratio according to specific applications. There is also evidence of negative and zero Poisson's ratio materials in biology.[11,36–42] To investigate cell-materials interactions, Poisson's ratio has to be precisely tuned, both in magnitude and polarity. Some tissue engineering applications require unique strain responses, wherein biomaterials having a negative or zero Poisson's ratio may be most suitable for emulating the behavior of native tissues. Recently, we developed micrometer-scale scaffolds which exhibit negative, positive and zero Poisson's ratio behavior in polyethylene diacrylate (PEGDA) biomaterials.[43–45] Although these scaffolds themselves exhibited NPR behavior, a single cell is not able to sense the effects of the altered Poisson's ratio at micrometer resolution ($\approx$50–100 $\mu$m). In this study, we develop a methodology to develop suspended structures ($\leq$1 $\mu$m) with tunable Poisson's ratios, which can be utilized to investigate cellular behavior.

## 3.3 Results and Discussion:

*3.3.1 Fabrication of Tunable Poisson's Ratio Scaffolds*

The re-entrant honeycomb unit cells design[34,46] was used to fabricate NPR

suspended structures (Figure 3.1E). The re-entrant structure is formed by changing the

four side angles (angle ζ) between the vertices (ribs) in a six-sided honeycomb (hexagon),

Two rib lengths, $L_1$ and $L_2$, constrain the dimensions of the unit-cell, including angle ζ

(the value of angle ζ is set by the rib-length ratio and is not arbitrarily set), and the ratio

of the two rib lengths has a sizable influence on Poisson's ratio. Varying angle ζ alters the

magnitude of Poisson's ratio, which gives Poisson's ratio its strain-dependent response.

We have simplified the re-entrant model, by setting $L_1 = L_2 = X = 8.3$ μm, which exhibits

a NPR response. Addition of an extra rib to the NPR design, inhibits free movements, and

transforms the structure to exhibit a PPR response. Femtosecond-laser-induced two-

photon polymerization was used to fabricate the NPR and PPR suspended web structures

using photosensitive PEGDA biomaterial (Figure 3.1B). PEGDA biomaterial was chosen,

because of its high water content and biocompatibility and tunable mechanical

properties.[3,47] Photosensitive prepolymer solution was prepared by adding biocompatible

initiator, lithium phenyl-2,4,6-trimethylbenzoylphosphinate (LAP),[48] and acrylate-PEG

RGDS peptide to 20% PEGDA solution. Methacrylated glass surface was coated with

PEGDA solution without the peptide, to prevent cell adhesion onto the glass surface. A

Ti:sapphire femtosecond laser was tightly focused onto the appropriate *z*-plane in the

volume of the PEGDA solution, and 3D structures were fabricated by moving the stage in

*x-y-z* directions. Structural support beams were incorporated at the ends of each web

structure to ensure that the structure is suspended, and cell will be able to apply strains

and freely move the structures. Similar NPR structures made on a flat surface can be actuated by addition/removal of water (Supporting Information Figure 3S1) and could be moved by the cells, however, the NPR structure movement could not be quantified in the absence of the supporting beams. Fixing the boundaries of the NPR structures also enables time-lapse imaging of cell movement and division. Visualization of the web-structures using scanning electron microscopy (SEM) resulted in collapsed web structures, even with critical point drying technique (Supporting Information Figure 3S2). As a result, the suspended structures were visualized by introducing PEG-RGD-FAM in the prepolymer solution [49] (Figure 3.1C). Fabrication methodology used in this work will be able to tune a wide range of elastic properties, by controlling the resolution of features via laser dosages, or by varying the prepolymer dilution (for example, mechanical properties of 80% NPR PEGDA structures will differ from both 20% NPR structures or 80% PEGDA slab structures). A 20 μm diameter glass colloidal particle attached to the atomic force microscopy (AFM) probe was used to compare the effective mechanical properties of NPR and PPR structures in the $z$-direction (Figure 3.1D). When a vertical forces is applied to the NPR web, the NPR features expand locally, yield, and conform to the bead surface, as opposed to the PPR web, which resists the vertical forces. This response possibly explains the significant differences in the mechanical properties between the NPR and PPR structures, even though both the structures were fabricated using 20% PEGDA.

*3.3.2 Characterization of Cell Response*

To evaluate cell response, 10T1/2 cells were seeded on the web structures and cell movement was captured using time-lapse microscopy. 10T1/2 are an anchorage dependent embryonic fibroblast cell line that differentiates into perivascular cells in vivo, typically used to stabilize a functional microvascular network. As cells move on NPR web structures, cells apply forces to their underlying substrate using focal adhesions, which deform the web in various configurations (Figure 3.2A). The web-points deformed by the cells return to their original positions when cells disengage and stop applying forces (Supporting Information Video S1). Cells are capable of deforming both NPR and PPR structures due to the intrinsic properties of a suspended web in a liquid medium. Due to its auxetic property, the NPR web responds and accommodates strains due to different cellular forces to a greater degree. When a NPR unit cell expands in the $x$- and $y$ directions: for every 0.9 μm $x$ displacement, there is a corresponding increase in $y$ by ≈8 μm (Figure 3.1E), which explains the larger $y$ displacement of web-point on NPR webs (Figure 3.2C). Cells can manipulate the PPR structures as well, however cells are not able to move the web-points to a greater degree (Figure 3.2B). For both the structures, there is some intrinsic movement, due to the suspended nature of the web in liquid medium (Figure 3.2D). The NPR web-points have the ability to move significantly more as compared to PPR web-points. The local yielding of NPR web due to cellular strains is a combination of rib bending (flexure), stretching, and hinging (angular deformations) of the position and arrangement of the ribs relative to each other.[31,34,46,50] The degree to which each structure deforms depends on unit cell geometry, the bulk material properties of the ribs and the direction of loading. According to the simple hinging model reported by Gibson and Ashby,[50] axial strain causes solely a change in angle ζ, while the

magnitude of the negative Poisson's ratio depends upon both $\zeta$ and the ratio $L_2/L_1$, where the rib length ratio is assumed to stay. However, since multiple cells apply forces in many different directions on the NPR web, the local Poisson ratio changes depending on proximity to cells and force transmission from other cells on the web. Some web points experience cellular pulling forces from adjoining cells on the web, while others experience inward pulling forces by the cell, and web-points with no cellular forces remain neutral. Since the Poisson ratio is calculated by measuring the transverse displacement of web points when axial forces are applied, for this particular case, it is difficult to measure the Poisson's ratio of the overall structure, since multiple cells apply forces on unit structures in a variety of $xy$ directions. Therefore, effective Poisson's ratios of unit NPR and PPR structures were calculated by selecting unit cells which deform by applying of cell-forces in either $x$- or $y$-axes, denoted by $\nu_{xy}$ and $\nu_{yx}$ (Figure 3.2E). The local expansion–contraction movement of the NPR web-points allows cellular force transmission. On the other hand, PPR web-points resist cellular forces to a greater degree and exhibit typical positive Poisson's ratio behavior. Careful control over cell concentration can be used to have single cell on each NPR web to precisely calculate local displacements and strains (Supporting Information Video S2). Structures from the literature, such as star honeycomb, chirals, rotating triangle or square units, structures formed from lozenge grids, etc., can be incorporated to design and tune biomaterials with precise strain-dependent NPR response.[51]

Immunofluorescence staining was carried out to evaluate cell adhesion and proliferation on both NPR and PPR web structures. On the NPR web, the cells seem to be randomly oriented, evident from actin staining (white arrow) (Figure 3.3A–C). The

pseudopods of the spread cells do not align along the suspended NPR struts. Cells on the

PPR web are not able to spread in the first two hours post-seeding, and most of the cells

adhere to the support structures (Supporting Information Video S3,4). Cells adhere to

both structures through integrin-mediated adhesions. Vinculin labeling is seen throughout

the cell structure and indicated small nascent adhesions while strong labeling on some of

the locations indicate larger (> 1 µm) focal adhesions. Cells proliferate well (≈ 100%) on

both PPR and NPR structures. Differences in focal adhesions between the NPR and PPR

structures were not significant. Tuning the size of the structures using varying laser

dosage and/or prepolymer concentration has the potential to be used as a way to have

direct control over adhesion sites. Cells seeded on NPR and PPR topologies attached to

the glass substrate also demonstrate high adhesion and proliferation (Supporting

Information Figure 3S3). Mechanical forces play an important role in cell division.[52]

Cell division, a critical aspect of all multicellular organisms, requires segregation of

chromosome facilitated by physical division of the cytoplasm, resulting in separate

daughter cells. In normal cell division, during telophase, the cleavage furrow ingresses

resulting in compression of the central spindle to form an intercellular microtubule bridge

called the midbody. The midbody is severed, resulting in the final separation of daughter

cells (Figure 3.3D). Time-lapse experiments revealed unusual cell division of 10T1/2

cells on NPR structures (Figure 3.3). On NPR webs, cleavage furrow ingression began

normally, however, the resulting daughter cells remain attached to each other for the

duration of the experiment (≈ 12 h). In one case, (Figure 3.3E–H) one cell resulted in

formation of a long structure, and probably underwent apoptosis after being unable to

complete abscission. In another case (Figure 3.3I–M), a cell underwent midbody

regressed after failing to separate, giving rise to a multinucleated cell. The cell then re-entered mitosis, however, the midbody persisted and did not break off throughout the duration of experiment. In one case, one of the nascent daughter cell was on top of the NPR web while the other was under the web, maintaining the midbody connection throughout the duration of the experiment. (Supporting Information Figure 3S4–6 and Video S5). Since cell division failure can cause genetic instability, ultimately leading to cancer[53] researchers have elucidated molecular mechanism of abnormal cell division using several midbody components. Cytokinesis failure and associated behavior has been reported following depletion of components of the cortical cytoskeleton, such as anillin, septins, and formins.[54–56] Our observations suggest that unusual cell division can be induced solely by the NPR structure, in absence of any external biochemical manipulations to the cell components. Fluorescent time-lapse images were also taken to monitor the nucleus activity of the cells using Hoechst 33342 (Supporting Information Figure 3S7). Arrows indicate symmetric as well as asymmetric furrow formation during cell division on NPR webs. During cell movement, bleb formation and constantly extending and retracting protrusions are also seen on the NPR web (Supporting Information Video S6,7). The NPR property affects the spatial distribution of adhesive contacts a cell experiences during cell division and movement, causing abnormal cell division.

## 3.4 Conclusion

Most tissue cells not only adhere to but also pull on their microenvironment and thereby respond to the mechanical properties of the substrates through cytoskeletal reorganization and associated processes. So far only one component of the mechanical property, the elastic modulus, has been investigated. This work potentially opens doors to fabricating biomaterials with tunable Poisson's ratio while keeping the bulk elastic modulus constant. We envision that this technique will be used to investigate effects of altering the Poisson's ratio on a variety of cellular aspects including morphology, gene expression, and migration using different cell types. Due to its importance in fundamental biological processes, such as tumor metastasis, wound healing and morphogenesis, cell migration has been extensive studied on a substrate with varying mechanical properties. Present understanding is that cellular forces are concentrated at focal adhesions (FA), whose size can be correlated to the amount of forces exerted by the cells on their underlying substrate. Recent reports acknowledge the fundamentally different cellular response on larger than micron and submicron scale features.[57] Methodology developed in this work, can control the resolution as well as have local yielding of the rib-structures thereby potentially controlling the size and spacing of FA sites. Cell response to a substrate with a gradient of elastic modulus[7] has also been investigated, and it is found that cells typically migrate preferentially toward stiffer regions. Similarly, a gradient Poisson's ratio structure can be fabricated (Supporting Information Figure 3S8), which will transmit cellular forces across a range of Poisson's ratio on a single substrate. A wealth of information about how cells apply forces has been gained by modulating the elastic modulus of the underlying substrate. It is expected that tuning the Poisson's ratio allows one to identify several components involved in mechanosensing. The platform

developed in this work will foster experiment and contribute to the broad field of
mechanobiology.

## 3.5 Experimental Section

### *3.5.1 Preparation of Sample Substrate*

Glass coverslips (Electron Microscopy Sciences, Hatfield, PA; 0.08–0.13 μm)
were cleaned for 5 min in piranha solution (35 mL sulfuric acid and 15 mL hydrogen
peroxide), washed 5 times with deionized (DI) water, and immersed in ethanol (5 min).
Methacrylation solution was prepared by mixing together 1 mL 3-(trimethoxysilyl)-
propyl methacrylate, 50 mL ethanol, and 6 mL of 1:10 glacial acetic acid (acetic acid in
ethanol). Dried coverslips were immersed in the methacrylation solution on a shaker
overnight, cleaned with ethanol and dried with compressed air. Methyacrylated glass
coverslips were coated with a thin layer of 20% PEGDA (80% water) as follows.
PEGDA solution was sandwiched between one piece of methacrylated coverslip and one
piece of untreated coverslip. The untreated coverslip was cleaned with ethanol before use.
A pipettor was used to transfer 7 μL PEGDA onto the surface of methacrylated coverslip
and the untreated coverslip was covered on top of the methacrylated coverslip. The
sandwich structure was placed on an experiment table for 3 min to stabilize, and
irradiated using a UV lamp (1 min) to polymerize the PEGDA layer and the two pieces
were detached. A 10 mm × 10 mm hole was cut on the bottom of a 35 mm plastic petri
dish with a single edge cutter blade and the PEGDA coated coverslip was glued

(dipentaerythritol pentaacrylate, Sartomer) with 1% photoinitiator (Irgacure 819) onto the bottom of the petri dish using UV polymerization.

*3.5.2 Femtosecond Laser Fabrication of the Webs*

Figure 3.1B shows the schematic drawing of the femtosecond laser fabrication system setup. The laser source was a Ti:sapphire femtosecond laser (Vitesse, Coherent Inc., Santa Clara, CA) producing 100-femtosecond wide pulses at a repetition rate of 80 MHz with a maximum power of 350 mW. The central wavelength of the laser was 800 nm and the diameter of the beam out of the laser head was 1 mm. The laser beam was expanded by a 4× beam expander to make full use of the aperture of the objective lens. Then the laser beam was guided by a group of mirrors into an inverted microscope (Nikon Eclipse Ti, Nikon Instruments Inc., Melville, NY) and focused by an oil-immersion objective lens (Plan Apo VC 100x, Nikon Instruments Inc., Melville, NY) onto the sample which was mounted on a motorized stage (Applied Scientific Instrumentation, Eugene, OR). The laser power could be continuously adjusted by an attenuator (NIR Polarizer, Edmund Optics Inc. Barrington, NJ). The scanning of the sample was implemented by simultaneously controlling the stage and an electrical-motorized shutter (Sutter Instrument Company, Novato, CA) using the microscope software. The laser power employed for the fabrication was 50 mW, measured by a power meter (PowerMax 500D, Molectron Detector Inc., Portland, OR) before the laser

beam enters the objective lens. The scanning process was monitored in situ by a charge-coupled device (CCD) camera (Qimaging, Surrey, BC, Canada).

Lithium phenyl-2,4,6-trimethylbenzoylphosphinate (LAP) photoinitiator was prepared as previously described.[48] Pre-polymer solution was prepared as follows. 20% PEGDA (MW 700, Sigma-Aldrich) was mixed with DI water (1:4, 4% (w/v)), LAP (2%), acrylate-PEG RGDS peptide (5 mM), and vortexed (5 min) and filtered using a 0.22 μm pore size syringe filter. Before making the structures, a drop of immersion oil was placed on the objective lens. A pipettor was used to place 20 μL of the 20% PEGDA on the bottom of the glass petri dish. The petri dish was then secured on the stage by two strips of double-side tape. A series of dots were made by the laser beam to locate the *z*-position of the coverslip surface. An array of seven supporting walls was fabricated. The supporting wall was an 8-layer wood-pile structure with the size of 120 μm (length) × 6 μm (width) × 12 μm (height) using stage speed of 0.05 mm/s and a laser power of 70 mW. Suspended NPR and PPR structures were fabricated with the sides of the structures attached to the supporting walls using a stage speed of 0.65 mm/s and laser power of 45 mW. Unpolymerized PEGDA was washed away using DI water, and the petri dish was filled with phosphate buffered saline (PBS) that contained 2% penicillin-streptomycin (PS), and stored at 37 °C. Fluorescence-labeled webs were fabricated using similar conditions using FAM-labelled PEG-RGD[49] (FAM 0.5 mg/mL)

*3.5.3 Time-Lapse Imaging*

10T1/2 cells (American Type Culture Collection, Manassas, VA) were maintained in Dulbecco's modified Eagle's medium with high glucose (DMEM) (Gibco, North Andover, MA) supplemented with 10% fetal bovine serum (FBS). The cells were cultured in an incubator with 5% $CO_2$ concentration and 37 °C. The culture medium was replenished every other day and the cells were split as necessary. Prior to cell seeding, the petri dish with the webs was washed twice with PBS. Then it was filled with 3 mL pre-warmed DMEM supplemented with 10% FBS and 1% PS. Throughout this process, caution was taken to keep the webs in liquid to prevent them from collapsing. An ethanol-washable marker was used to mark the position of the webs on the bottom of the petri dish to facilitate cell seeding. A drop of 10 μL medium (seeding density: 5000 cells per petri dish) was carefully added on top of the webs.

Time-lapse images were taken in a microscope (Nikon) with a cell culture chamber (In Vivo Scientific Inc.) after the cells were seeded on the webs. The $CO_2$ concentration and the temperature in the cell culture chamber were maintained at 5% and 37 °C, respectively. The bottom of the chamber was filled with DI water to maintain the humidity. The heater of the chamber was turned on 4 h before the time-lapse imaging to achieve a stable 37 °C environment. A 40× objective lens was used to take the time-lapse images every 2 min at a range of $z$-positions with a step of 2 μm. With the same setup, fluorescent time-lapse images were taken to monitor the nucleus activity of the cells using Hoechst 33342 (1 μg/mL).

*3.5.4 Immunofluorescence Labeling*

EdU staining was conducted with the Click-iT EdU imaging kit (Invitrogen, Carlsbad, CA) following the protocol provided by the manufacturer. After the cells were seeded on the web for 12 h, EdU was added into the medium at 10 μM and the cells were cultured in the incubator for another 12 h. After the incubation, the medium was removed and the sample was fixed with 0.5 mL of 4% formaldehyde in PBS for 15 min at room temperature. Formaldehyde was removed and the petri dish was rinsed twice with 1 mL of 2% BSA in PBS for 5 min each. After being permeablized with 1 mL of 0.5% Triton X-100 in PBS for 20 min, the sample was again rinsed twice with 1 mL of 2% BSA in PBS for 5 min each. Then the sample was incubated in the Click-iT reaction cocktail which contained Click-iT reaction buffer, $CuSO_4$ , Alexa Fluor azide, and reaction buffer additive for 30 min at room temperature, protected from light. After the reaction cocktail was removed, the sample was rinsed once again with 1 mL of 2% BSA in PBS for 5 min.

The sample was incubated with 2 mL of 5 μg/mL Hoechst 33342 in PBS for 30 min at room temperature for DNA staining. Hoechst solution was removed and the sample was washed twice with 3 mL of PBS. For focal adhesion staining, the sample was first blocked for 60 min in blocking buffer containing 2% BSA, 0.3% Triton X-100, and 97.7% PBS. Primary antibody solution, (0.5% monoclonal anti-vinculin, Sigma, in blocking buffer), was applied onto the sample and the sample was incubated overnight at 4 °C. Sample was rinsed and incubated in the secondary antibody solution (1% Alexa Fluor 647 goat anti-mouse IgG in blocking buffer) for 60 min at room temperature. Cell nucleus, proliferation (EdU), actin filaments, and focal adhesion architecture were

examined by immunofluorescence confocal microscopy. Cell were stained for nuclear DNA, proliferation marker EdU, focal adhesion protein vinculin, and cytoskeletal filamentous actin. 3D image stacks were acquired using a confocal system (Olympus FV1000) mounted on an Olympus IX81 inverted optical microscope. 3D images were processed using a combination of Volocity imaging software and Image J (National Institute of Health).

*3.5.5 Strain Analysis*

Time-lapse images were digitized and *x*- and *y*-displacements of various webpoints were determined based on the undeformed in-plane dimensions of the structures. Since webpoints on NPR and PPR structure experienced forces in different directions from multiple cells, effective Poisson's ratios of individual unit-cells were calculated. Unit cells were chosen where cells apply forces in either *x*- or *y*-directions. The transverse elastic deformation of the unit NPR and PPR webpoints was calculated by resulting strains (in *x*- or *y*-directions). Axial and transverse strains and Poisson's ratios of selected unit cells were estimated by measuring the displacement of webpoints, using Equation 1.[58]

$$v_{xy} = -\frac{\varepsilon_y}{\varepsilon_x} \qquad v_{yx} = -\frac{\varepsilon_x}{\varepsilon_y} \qquad (1)$$

where $\upsilon_y$ and $\upsilon_x$ are strains in $y$-and $x$-directions. In-plane values of Poisson's ratio resulting from in-plane cellular strains were calculated using a 2D Cartesian coordinate system with orthogonal $x$- and $y$-axes

### 3.5.6 Effective Stiffness

The AFM indentation studies were performed with a commercial instrument (multimode microscope, Veeco Inc., Digital Instruments, Santa Barbara, CA) mounted on an inverted optical microscope. This set-up enabled the positioning of the AFM tip on the NPR and PPR regions of the suspended web structures. A standard sharp silicon nitride tip could not be used, because of the nature of the open suspended web structures. Soft contact tips (PNP-TR silicon nitride probe) with a 20 μm diameter glass colloidal particle (force constant ≈0.08 N/m), was used for all force measurements. Force curves were taken on each web structure using a 4 × 4 grid array (16 points per web, three PPR and NPR webs with varying indentation depths) in aqueous mode using a fluid cell with PBS at room temperature. Force curve data were extracted from AFM files and analyzed off-line. The Young's modulus ($E$) was computed from approaching force curves using a Hertzian model with any arbitrary two points, $(z_1,d_1)$ and $(z_2,d_2)$, on the force curve, using the following equation:

$$\frac{1}{E} = \left[ \frac{(z_1 - z_2) - (d_1 - d_2)}{\left(\frac{3k(1-v^2)}{4\sqrt{R}}\right)\left((d_1 - d_2)^{\frac{2}{3}} - (d_2 - d_0)^{\frac{2}{3}}\right)} \right]$$

where $\upsilon$ is the Poisson ratio (since the force was applied in $z$-direction and Poisson's ratio was altered in the $x$-$y$ plan, the Hertz model was used and the Poisson's ratio was 0.3); $k$ is the spring constant of cantilever, $R$ is the tip radius (10 μm). $E$ was determined using the entire region of the compression curve, averaging values by using a five-point moving filter (slope of the curve every 5 points).

Chapter 3, in full, is a reprint of the material as it appears in Advanced Function Materials 2013. Zhang, W., Soman, P., Meggs, K., Qu, X., & Chen, S. are the co-authors of this material.
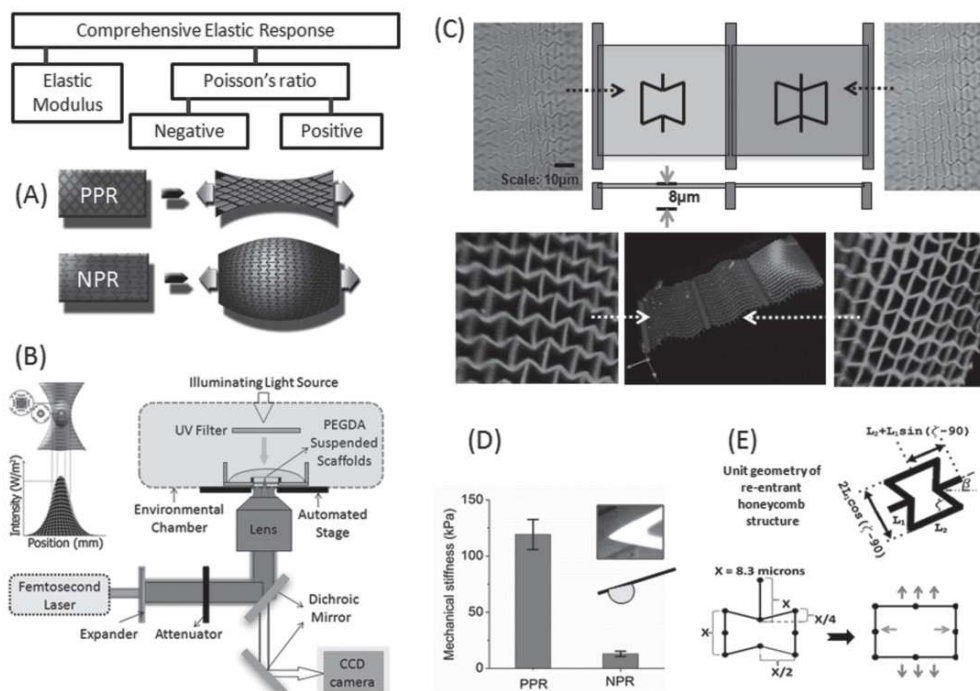
Figure 3.1. The elastic property of a biomaterial can be comprehensively expressed by the elastic modulus and the Poisson's ratio. Schematic shows a PPR material contracting transversally when axially stretched, while a NPR material expanding in both the axial and transverse directions. B) Schematic of the two-photon absorption process and the femtosecond laser fabrication set-up. C) Optical and confocal images of NPR and PPR suspended web structures with side supports using PEGDA biomaterial. D) AFM measurements using a 20 $\mu$ m bead measures the effective stiffness of NPR and PPR web structures in the z-direction. E) Re-entrant honeycomb configuration was adopted as the unit cell geometry for the NPR web, while an additional strut modification to the NPR structure served as the positive control. Schematic shows biaxial expansion of the NPR structure upon axial strains (arrows).
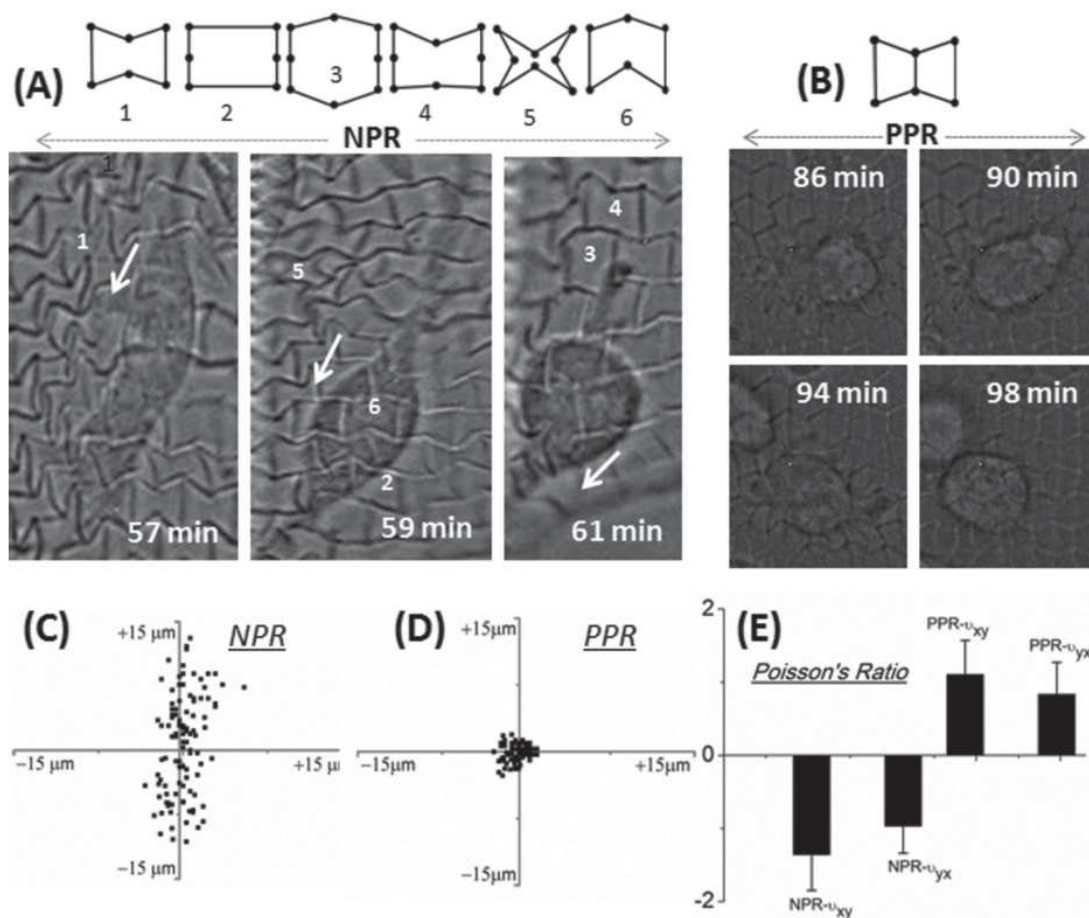
Figure 3.2. The suspended structure exhibits a combination of rib bending or flexure, stretching, and hinging (angular deformations) as a 10T1/2 cell moves across the web structure (1–6). White arrows indicate the direction of movement with associated time stamps. B) The PPR web structure resists cells movements. C,D) Frame-to-frame trajectory of multiple webpoints after 10T1/2 cell seeding on PPR and NPR structures. Data pooled from different locations on the web structures for 2 h with 8 min intervals. Web-points of the NPR structures move significantly more as compared to PPR web-points. E) Graph shows effective Poisson's ratio upon cellular strains in the x- and y-directions.
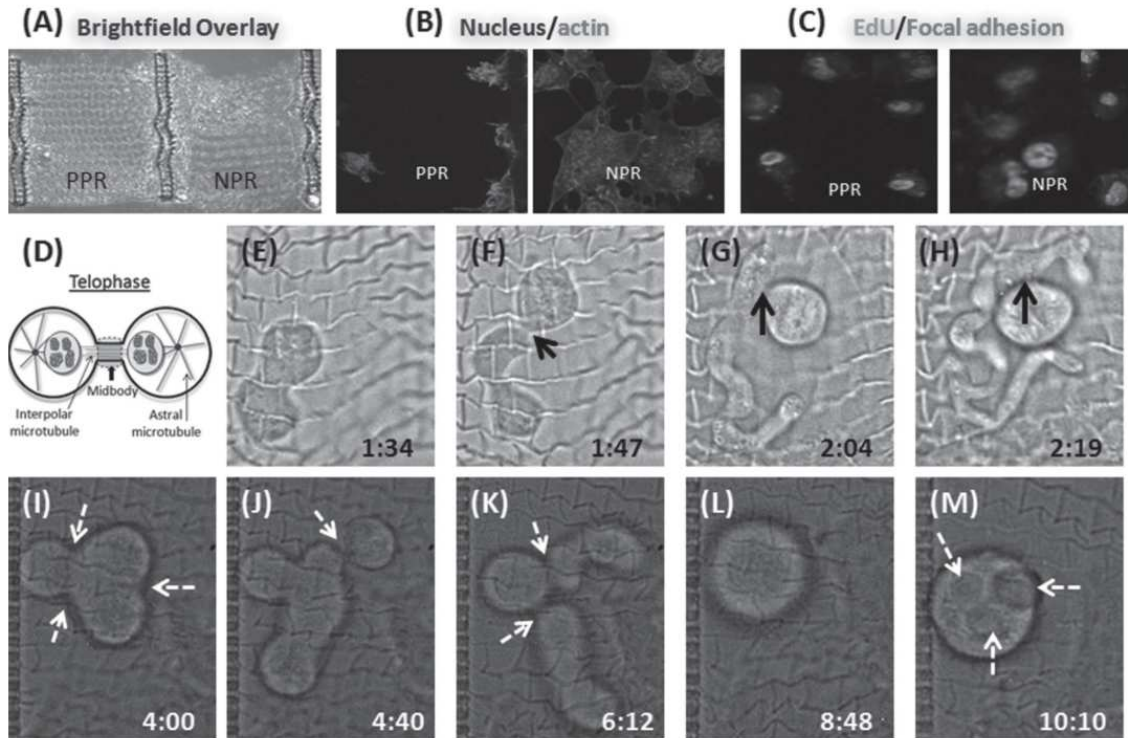
Figure 3.3. A–C) Immunostaining of 10T1/2 cells for adhesion (nucleus, actin, and focal adhesions) and proliferation (EdU). D) Schematic illustration showing cell in telophase: the cleavage furrow ingresses, compresses the midzone, and creates an intercellular bridge containing a microtubule midbody. In normal cell division, the bridge is resolved creating two daughter cells. The NPR structure induces aberrant cell-division response: E–H) Abnormal cell-division initiates and results in the formation of a long structure. Black arrow indicates persistent mid-body connection. I–M) Multiple sites of symmetric as well as asymmetric furrow formation during cell division on the NPR webs (dotted white arrows).

## 3.6 References

1. J. P. Butler , I. M. Tolic-Norrelykke , B. Fabry , J. J. Fredberg , *Am. J. Physiol. Cell Physiol.* 2002 , *282* , C595.

2. M. Dembo , Y.-L. Wang , *Biophys. J.* 1999 , *76* , 2307 .

3. Khademhosseini , R. Langer , *Biomaterials* 2007 , *28* , 5087 .

4. D. E. Discher , P. Janmey , Y.-l. Wang , *Science* 2005 , *310* , 1139.

5. P. A. Janmey , J. P. Winer , M. E. Murray , Q. Wen , *Cell Motil. Cytoskeleton* 2009 , *66* , 597 .

6. R. J. Pelham , Y.-l. Wang , *Proc. Natl. Acad. Sci. USA* 1997 , *94* ,13661 .

7. C.-M. Lo , H.-B. Wang , M. Dembo , Y.-l. Wang , *Biophys. J.* 2000 , *79* ,144 .

8. J. Engler , S. Sen , H. L. Sweeney , D. E. Discher , *Cell* 2006 , *126* , 677 .

9. M. J. Paszek , N. Zahir , K. R. Johnson , J. N. Lakins , G. I. Rozenberg ,A. Gefen , C. A. Reinhart-King , S. S. Margulies , M. Dembo ,D. Boettiger , D. A. Hammer , V. M. Weaver , *Cancer Cell* 2005 , *8* , 241 .

10. N. Huebsch , P. R. Arany , A. S. Mao , D. Shvartsman , O. A. Ali ,S. A. Bencherif , J. Rivera-Feliciano , D. J. Mooney , *Nat. Mater.* 2010 ,*9* , 518 .

11. J. L. Williams , J. L. Lewis , *J. Biomech. Eng.* 1982 , *104* , 50 .

12. N. R. Keskar , J. R. Chelikowsky , *Nature* 1992 , *358* , 222 .

13. R. H. Baughman , J. M. Shacklette , A. A. Zakhidov , S. Stafstrom ,*Nature* 1998 , *392* , 362 .

14. D. J. Gunton , G. A. Saunders , *J. Mater. Sci.* 1972 , *7* , 1061 .

15. R. H. Baughman , D. S. Galvao , *Nature* 1993 , *365* , 735 .

16. G. B. Gardner , D. Venkataraman , J. S. Moore , S. Lee , *Nature* 1995 ,*374* , 792 .

17. L. J. Hall , V. R. Coluci , D. S. Galvao , M. E. Kozlov , M. Zhang ,S. O. Dantas , R. H. Baughman , *Science* 2008 , *320* , 504 .

18. R. Lakes , *Science* 1987 , *235* , 1038 .

19. J. B. Choi , R. S. Lakes , *J. Mater. Sci.* 1992 , *27* , 5375 .

20. J. B. Choi , R. S. Lakes , *J. Mater. Sci.* 1992 , *27* , 4678 .

21. G. W. Milton , *J. Mech. Phys. Solids* 1992 , *40* , 1105 .

22. K. L. Alderson , K. E. Evans , *Polymer* 1992 , *33* , 4435 .

23. B. D. Caddock , K. E. Evans , *J. Phys. D Appl. Phys.* 1989 , *22* ,1877 .

24. K. E. Evans , B. D. Caddock , *J. Phys. D Appl. Phys.* 1989 , *22* ,1883 .

25. R. H. Baughman , S. O. Dantas , S. Stafstrom , A. A. Zakhidov , T. B. Mitchell , D. H. E. Dubin , *Science* 2000 , *288* , 2018 .

26. R. Lakes , *Science* 2000 , *288* , 1976 .

27. K. E. Evans , A. Alderson , *Adv. Mater.* 2000 , *12* , 617 .

28. R. Lakes , *Nature* 1992 , *358* , 713 .

29. S. Burns , *Science* 1987 , *238* , 551 .

30. R. H. Baughman , S. Stafstram , C. Cui , S. O. Dantas , *Science* 1998 , *279* , 1522 .

31. K. E. Evans , M. A. Nkansah , I. J. Hutchinson , S. C. Rogers , *Nature* 1991 , *353* , 124 .

32. L. Rothenburg , A. I. Berlin , R. J. Bathurst , *Nature* 1991 , *354* , 470 .

33. J. B. Choi , R. S. Lakes , *J. Compos. Mater.* 1995 , *29* , 113 .

34. L. J. Gibson , M. F. Ashby , G. S. Schajer , C. I. Robertson , *Proc. R. Soc. London, Ser. A* 1982 , *382* , 25 .

35. R. F. Almgren , *J. Elast.* 1985 , *15* , 427 .

36. X. G. Chen , G. W. Brodland , *J. Mech. Behav. Biomed. Mater.* 2009 , *2* ,494 .

37. L. H. Timmins , Q. F. Wu , A. T. Yeh , J. E. Moore , S. E. Greenwald , *Am. J. Physiol.–Heart Circ. Physiol.* 2010 , *298* , H1537 .

38. G. Burriesci , G. Bergamasco , US patent 162112, 2007 .

39. Y. Lin , N. Kikuchi , S. J. Hollister , *J. Biomech.* 2004 , *37* , 623 .

40. R. Lakes , *Nature* 2001 , *414* , 503 .

41. R. J. Jackman , S. T. Brittain , A. Adams , M. G. Prentiss ,G. M. Whitesides , *Science* 1998 , *280* , 2089 .

42. R. Veronda , R. A. Westmann , *J. Biomech.* 1970 , *3* , 111 .

43. P. Soman , D. Y. Fozdar , J. W. Lee , A. Phadke , S. Varghese , S. Chen , *Soft Matter* 2012 , *8* , 4946 .

44. P. Soman , J. W. Lee , A. Phadke , S. Varghese , S. Chen , *Acta Biomater.* 2012 , *8*, 2587.

45. Y. Fozdar , P. Soman , J. W. Lee , L.-H. Han , S. Chen , *Adv. Funct. Mater.* 2011 , *21* , 2712 .

46. I. G. Masters , K. E. Evans , *Compos. Struct.* 1996 , *35* , 403 .

47. J. Y. Lee , D. J. Mooney , *Chem. Rev.* 2001 , *101* , 1869 .

48. B. D. Fairbanks , M. P. Schwartz , C. N. Bowman , K. S. Anseth , *Biomaterials* 2009 , *30* , 6702 .

49. M. S. Hahn , L. J. Taite , J. J. Moon , M. C. Rowland , K. A. Ruffi no , J. L. West , *Biomaterials* 2006 , *27* , 2519 .

50. J. Gibson , M. F. Ashby , *Cellular solids: structure and properties* , Cambridge University Press , Cambridge, UK 1997 .

51. N. Greaves , A. L. Greer , R. S. Lakes , T. Rouxel , *Nat. Mater.* 2011 , *10* , 823 .

52. T. Itabashi , Y. Terada , K. Kuwana , T. Kan , I. Shimoyama , S. i. Ishiwata , *Proc. Natl. Acad. Sci. USA* 2012, *109*, 7320 .

53. T. Fujiwara , M. Bandi , M. Nitta , E. V. Ivanova , R. T. Bronson , D. Pellman , *Nature* 2005 , *437* , 1043 .

54. P. Estey , C. Di Ciano-Oliveira , C. D. Froese , M. T. Bejide , W. S. Trimble , *J. Cell. Biol.* 2010 , *191* , 741 .

55. S. O. Dean , S. L. Rogers , N. Stuurman , R. D. Vale , J. A. Spudich , *Proc. Natl. Acad. Sci. USA* 2005 , *102* , 13473 .

56. F. Straight , C. M. Field , T. J. Mitchison , *Molec. Biol. Cell* 2005 , *16* ,193 .

57. S. Ghassemi , G. Meacci , S. Liu , A. A. Gondarenko , A. Mathur , P. Roca-Cusachs, M.P. Sheetz , J. Hone , *Proc. Natl. Acad. Sci. USA* 2012 .

58. M. M. Eisenstadt , *Introduction to mechanical properties of materials* , Macmillan, New York 1971 .

# Chapter Four:  Three-dimensional Cell Patterning by Ultrafast Laser-Induced Degradation of Collagen Hydrogels

## 4.1 Abstract

We report a methodology for three-dimensional cell patterning through ultrafast laser induced degradation (ULID) in a hydrogel in situ. Gold nanorods within a cell-encapsulating collagen hydrogel absorb a focused near-infrared femtosecond laser beam, locally degrading the collagen and forming channels, into which endothelial cells migrate, align, and eventually form tube-like structures, similar to the formation of micro-vessels. Pattern resolution can be tuned by writing speed, nanorod concentration, collagen concentration, and laser power. ULID presents a flexible, one-step, direct-write method that can be broadly applicable in 3D tissue engineering systems requiring spatial cellular patterning, especially those creating microvasculature.

## 4.2 Introduction

Tissue engineering offers the ability to generate functional tissues for implantation and in vitro modeling.[1] Three-dimensional (3D) cellular organization is critical to the function of a given tissue, and moreover, vascular integration plays a crucial role in providing nutrient and gas transport to the rest of the tissue.[2-6] Thus, materials that enable 3D organization of the tissue and its vasculature are of high

39

importance.[7, 8] Hydrogels – water-swollen polymer networks - are extensively used as the scaffolding in engineered tissues.[9] There are various ways to control hydrogel structure in 3D for the purpose of dictating cellular organization. 3D printing, which includes extrusion, stereolithography, and projection printing, builds hydrogel structures in an additive fashion.[10-12] Oppositely, the selective removal of material from a bulk gel (for instance, using a ultrafast laser) can also generate 3D structures with precise architecture.[13, 14] To this end, we developed a novel 3D patterning method - ultrafast laserinduced degradation (ULID) – to pattern hydrogels that can be spatially degraded to promote cell recruitment, alignment, and ultimately vascular tube formation in vitro. The hydrogel is composed of collagen with gold nanorods that absorb NIR light at their plasmon resonance to photothermally degrade the collagen and create internal channels. Photothermal activation in temperature-sensitive materials has previously been explored for triggered drug release, bulk hydrogel degradation, and 2D hydrogel patterning. [10, 15, 16] Here, we report for the first time its utility in 3D hydrogel patterning. Patterning takes place within *milliseconds* and can be tuned by the laser writing speed, gold nanorod concentration, collagen concentration and laser power. We empirically determined the optimal parameters to achieve high cell viability and reproducible patterning that enables vascular tube formation, making this ULID platform a viable alternative for cellular patterning in 3D, as well as an important step towards creating microvasculature in tissue engineered hydrogels.

## 4.3 Results and Discussion

Collagen hydrogels with gold nanorods displayed an absorbance profile similar to that of the nanorods in solution (Figure 4.2A), peaking at 800nm – coinciding with the wavelength of the NIR femtosecond laser. Collagen hydrogels without nanorods, conversely, showed low absorbance at 800 nm. When exposed to maximum power and the slowest speed (290 mW, 0.25 mm/s), collagen hydrogels without nanorods (collagen – NR) showed no changes in hydrogel morphology and resulting cell organization, suggesting the gold nanorods played a key role in the patterning mechanism (Supplemental Figure 4.5). Figure 4.2B displays a computer-designed pattern using ULID on a collagen-NR hydrogel and the resulting image using brightfield microscopy.

Internal patterning of the collagen-nanorod hydrogel was a modular process, where laser power and writing speed (in millimeters per second, mm/s) altered the diameter of the resulting channel pattern. Figure 4.3A displays brightfield images of the resulting patterns in the collagen gel exposed to 100 mW or 150 mW laser power, at laser scanning speeds of 0.25 mm/s, 0.75 mm/s, or 2.0 mm/s. Figure 4.3B shows the graphical representation of this data. An inverse relationship exists between the writing speed and pattern width. Laser power determines the threshold pattern size, where 100mW can generate $8.7 \pm 0.5$ µm resolution patterns (equal to the diameter of the laser beam) while higher powers such as 150mW and 190mW plateaued at $56.7 \pm 3.0$ µm and $128.6 \pm 9.3$ µm, respectively. Patterns made with 290mW power were barely distinguishable as the response in the collagen gel degraded the entire construct, however at a speed of 2.0 mm/s, the resolution was roughly $179.3 \pm 23.5$ µm. Writing speeds greater than 2.0 mm/s were not possible due to limitations with the automated stage, but presumably the

patterns could become even more optically defined with faster speeds.

For cell studies, collagen-nanorod hydrogels with bend3 endothelial cells at a concentration of 1000 cells per μl were used. We patterned channels using various powers and writing speeds and performed a fluorescent live/dead assay with calcein AM/ethidium homodimer (Figure 4.4A). We believe collagen degradation is occurring because the cells appear loose and mobile in the patterned region upon irradiation of the NIR light. (Supplementary Video 1). Ultimately, we chose a writing speed of 2.0 mm/s and a laser power of 100 mW for the remaining cell experiments due to their high pattern fidelity and high cell viability (>90%). We allowed collagen gels to incubate for several weeks, during which we observed cell migration towards the patterns, cell elongation on the walls, and by day 7 demonstrated hollow tube formation (Figure 4.4B). We confirmed that the channels were inducing this cellular organization by comparing with hydrogels without patterns (Supplementary Figure 4.6). It is clearly shown that the patterns induce cellular tube formation.

To further confirm this phenomena, the gels were fixed and stained for actin and nuclei and imaged using confocal microscopy. Using Volocity 3D reconstruction software (PerkinElmer Inc), we were able to visually observe the tube structure (Figure 4.4C), and XY and YZ planes confirmed the tubes length and hollow nature (Figure 4.4C outset). These data suggest tube formation occurred along the hollowed degraded channel and that endothelial cells populated the channel walls, forming hollow tubes similar to vessel formation in vasculogenesis.

The concept of spatially degrading a hydrogel for directing cellular response has been previously explored.[14] Groups have developed photolabile materials that respond

to UV or visible light. One disadvantage of these systems, however, is the relatively long timescale – in minutes – to achieve patterning. Another disadvantage is that the shorter wavelengths (<600nm) are damaging to cellular content, since water absorbs more light in those wavelengths. Here we demonstrated hydrogel patterning with NIR light as a more benign way to pattern hydrogels as it is minimally absorbed by water.[17] The efficient absorption of NIR light by the gold NRs and subsequent photothermal degradation of collagen allows for rapid patterning and minimizes cell exposure and thus potential for cell damage. We previously demonstrated a method to pattern gold nanorod-hydrogel substrates in 2D, [16] however, to our knowledge, this concept has not yet been explored in 3D hydrogel patterning. Additionally, it was previously demonstrated that hydrated collagen (similar to our collagen hydrogel) degrades at 55˚C.[18] Thus, it can be interpreted that our patterns are momentarily (i.e. for milliseconds) heating up to this temperature during patterning before returning to sink conditions of 37˚C. Below a certain threshold (e.g. patterning at 50mW and 2.0 mm/s) we see no pattern and resulting cell response. Therefore we believe the collagen is not degrading in this instance (Supplementary Figure 4.5).

As with any new fabrication/materials/ process, finding an application for NR induced hydrogel degradation is key. We found that a combination of the right parameter of nanorod concentration, collagen material, laser speed, and laser power allowed for fabrication of 3D channels inside a pre-made collagen encapsulating cell network with very little cell damage. Using a programmable 3D stage allows for complex vascular tube formation. Vasculogenesis within hydrogels has remained a hurdle for achieving tissues of scale for implantation and biomimetic tissue models for in vitro studies. Previously,

only a few groups have reported guidance of tube formation using labor-intensive techniques such as micromolding and casting.[19, 20] Here, we demonstrated a facile, one-step process that instantaneously degrades channels within the hydrogel, allowing for on-demand cell patterning. We not only showed endothelial cell migration and elongation on degraded channels, but confocal microscopy confirmed that hollow tube formation had occurred after a week, with the tubes elongating over several weeks after. This result could be interpreted as a breakthrough in the vascularization of tissue engineering systems and could be broadly implemented in many different tissues and models.

One such model that stands to benefit from this novel process is an angiogenesis model, whereby the creation of vascular tubes and subsequent seeding of a second cell type (e.g. cancer) can provide a facile means of studying angiogenesis between the two cell populations. Another possibility is to implement this platform with more complex vascular structures in hopes of guiding a biomimetic cellular organization in vitro. We believe this platform may also be generally applicable to many cell types that require cellular organization in 3D, making it versatile and robust for tissue engineering systems. Lastly, while we showed complete collagen degradation, it may be achievable to incur partial degradation – or uncrosslinking – of the collagen network, or utilize a material whose degradation occurs at lower temperatures (closer to 37˚C) – which could allow for additionally altered cell responses.

## 4.4 Conclusion

The described platform – ultrafast light-induced degradation (ULID) of hydrogels – allows for the patterning of internal channels in collagen hydrogels *in situ*, in this case enabling microvasculature formation. Alignment of nearby cells can be visualized as early as 1 day post-patterning, while migration and tube formation may take up to 14 days. This platform has broad applications in *in vitro* cell patterning and can be applied to a host of light-responsive materials in addition to collagen. Furthermore, more complex patterns could be implemented to achieve a higher degree of 3D patterning.

## 4.5 Experimental

### 4.5.1 Materials

For gold nanorods, hydrochloroauric acid (HAuCl$_4$), silver nitrate (AgNO$_3$), sodium borohydride (NaBH$_4$), and L-ascorbic acid were purchased from Sigma-Aldrich and cetyltrimethylammonium bromide (CTAB) was purchased from CalBioChem (EMD Millipore). Milli-Q water (18.2 Ω, MilliPore) was used in all synthesis steps. mPEG-thiol (5 kDa) (Nanocs) was used in nanorod surface modification. For hydrogels, collagen I, High Concentration (8.7 mg/mL) (VWR) was purchased.

### 4.5.2 Gold Nanorod Synthesis and Surface Modification

Gold nanorods were synthesized and using a seed-mediated growth and surface-modification methodology as previously described with some modifications.[21] 7.5mL 0.1M of CTAB was mixed with 250μL 0.01M HAuCl$_4$, followed by addition of 600μL

0.01 NaBH$_4$. Seeds formed after 2 minutes of mixing. The growth solution was prepared by mixing 40mL of 0.1M CTAB, 1.7 mL 0.01M HAuCl$_4$, 250µL of 0.01 AgNO$_3$, and 270 µL of 0.1M L-ascorbic acid, followed by 420µL of the seed solution. Nanorods formed after several hours. Nanorods were surface modified by first centrifuging twice at 15,000 $g$, removing the supernatant and resuspending in diH$_2$O, followed by adding mPEG-SH dropwise and allow to gently mix for 2 hours. Nanorods were again pelleted and washed in diH$_2$O to remove excess reactants and sterilized through a 0.22 µm filter for later use. Final nanorod concentration was determined to be 5.45 e-9 M, by absorbance readings at its plasmon resonance (~800nm).

### 4.5.3 Cell Culture

Bend3 mouse endothelial cells were used for cell culture experiments. Bend3 were grown in EGM-2 media (Lonza) and passaged several times after thawing. In preparation for collagen gel experiments, cells were trypsinized in 0.25% trypsin-EDTA, pelleted and resuspended in EGM-2 at various concentrations (1.0 million/mL up to 5 million/mL).

### 4.5.4 Gelation of Collagen-nanorod hydrogels

Collagen gels were formed using the manufacturer's instructions. Briefly, an ice-cold mixture of 1.04µL of 1N NaOH, 10µL 10x dPBS, and 10 µL of nanorods at their final concentration was prepared. Next, 33 µL of either diH$_2$O or cells at various concentrations (in EGM-2) was added, again kept at 4 degrees. 46 µL of stock Collagen I

(8.7 mg/mL) was added to the solution and pipetted slowly to mix the contents without producing air bubbles. The mixed solution was then added to 35 mm glass-bottom dishes with 10 mm wells (#0 cover glass, In Vitro Scientific) and placed in the incubator (37 degrees C, 5.0% $CO_2$) for 30 minutes. Following gelation, 2 mL of warmed EGM-2 media was added for cell culture.

*4.5.6* In Vitro *Hydrogel Patterning with bend3 Endothelial Cells*

Gels were immediately used for patterning following gelation and addition of warmed media. The glass dishes were placed on an automatic stage atop an inverted microscope (Olympus). A femtosecond laser beam (100 femtoseconds, 800 nm wavelength, 80 MHz, Coherent) was used to pattern the samples. The laser was focused through the laser objective lens (10x, NA 0.45) and onto the gel sample. Patterns were drawn inside the hydrogels by varying the focal plane of the beam (in z-direction) and according to digital masks designed on the computer, with controlled writing speeds (mm/s) using the stage controller (MS2000, ASI). Average power of the laser beam was modulated using an attenuator, varying the power from 100 - 290 mW, read by a power meter (Coherent Fieldmax).

Chapter 4, in full, is in preparation for submissions as: Hribar, K., Meggs, K., Liu, J., Qu, X., & Chen, S. Three Dimensional Cell Patterning by Ultrafast Laser-Induced Degradation of Collagen Hydrogels.
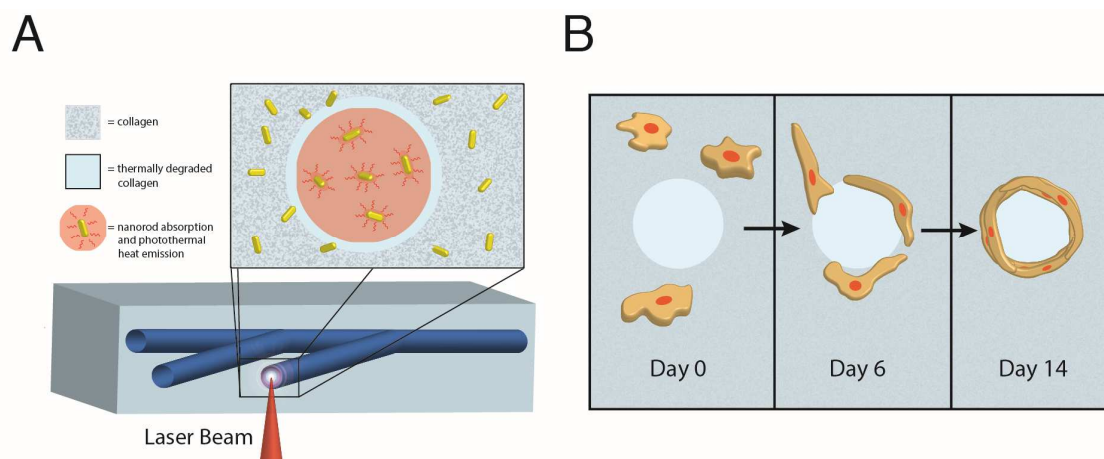
Figure 4.1. Schematic of the ULID patterning process and resulting cell response. A) A near-infrared (NIR) laser is focused inside the optically clear hydrogel and triggers the photothermal degradation of the collagen internally according to a computer-generated design, thereby creating channels. B) Expected cell response to degraded channels, where cells migrate towards the channels, align, and eventually form tubular structures with hollow cores, resembling microvasculature.
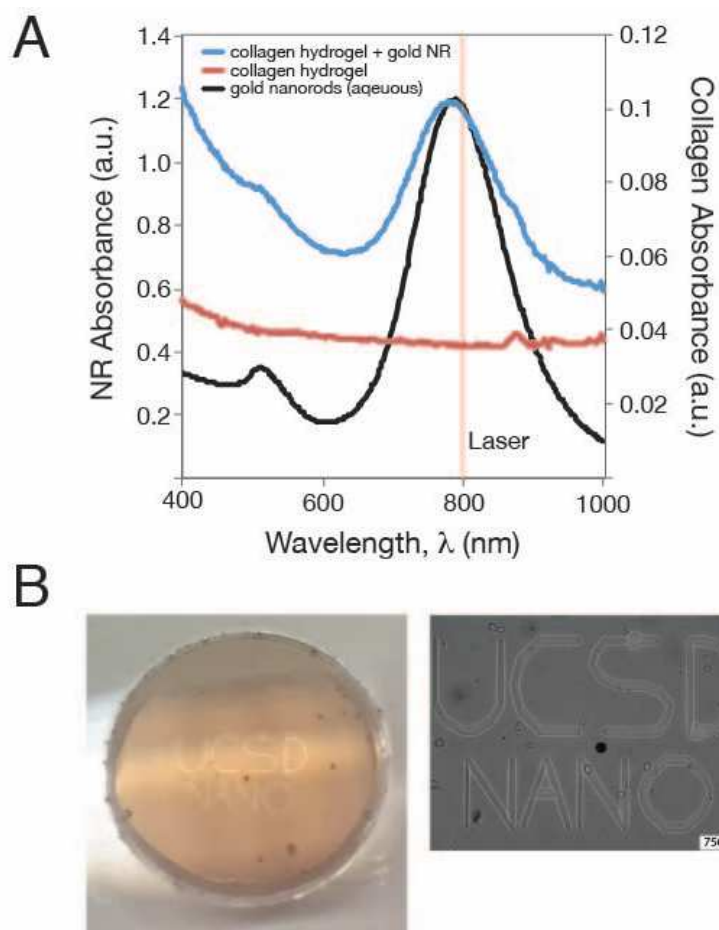
Figure 4.2. Characterization of materials. A) Absorbance of collagen hydrogels with and without nanorods, compared to nanorods in aqueous solution. The laser wavelength is also highlighted (800 nm). B) Image of gel within the glass dish, with outset showing a visible pattern. C) brightfield image of the same pattern.
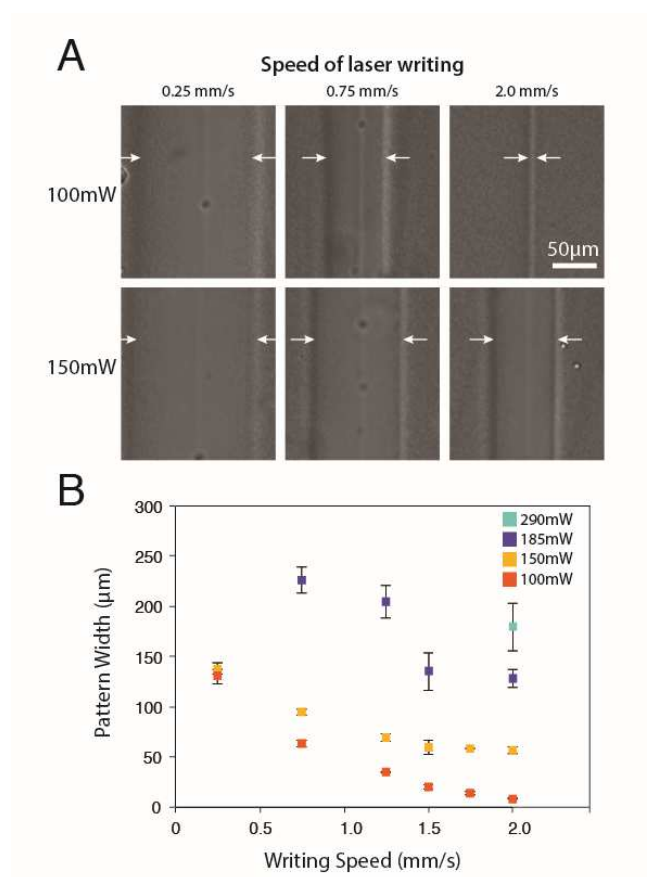
Figure 4.3. Characterization of the patterning. A) Brightfield images of the patterned lines at different writing speeds (0.25, 0.75, and 2.0 mm/s) and laser powers (100 and 150 mW). B) Characterization of patterned line widths in response to various writing speeds and laser powers.
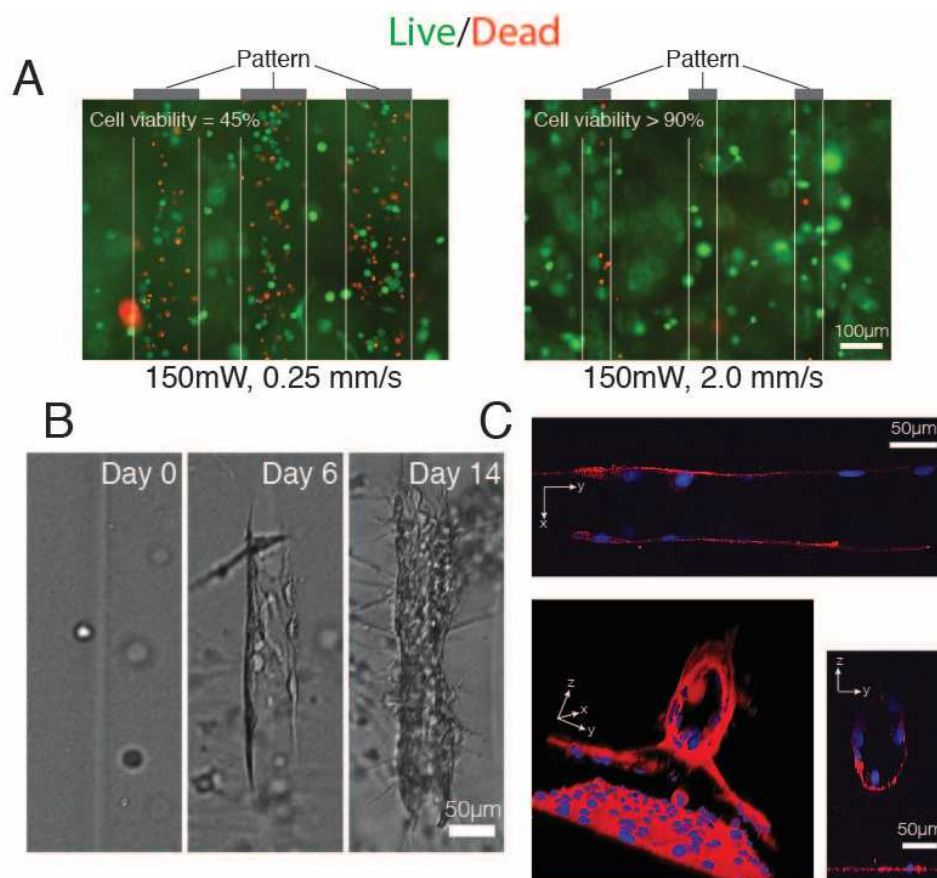
Figure 4.4. Endothelial cell response to 3D patterning. A) Live/dead fluorescent images overlayed with brightfield images, denoting differences in cell viability according to different writing speeds (0.25 and 2.0 mm/s) at 150mW laser power. B) Cell migration and tube formation, visualized in brightfield. C) endothelial tube formation visualized with confocal, showing hollow cores in the YZ plane and aligned endothelial cells in the XY plane.
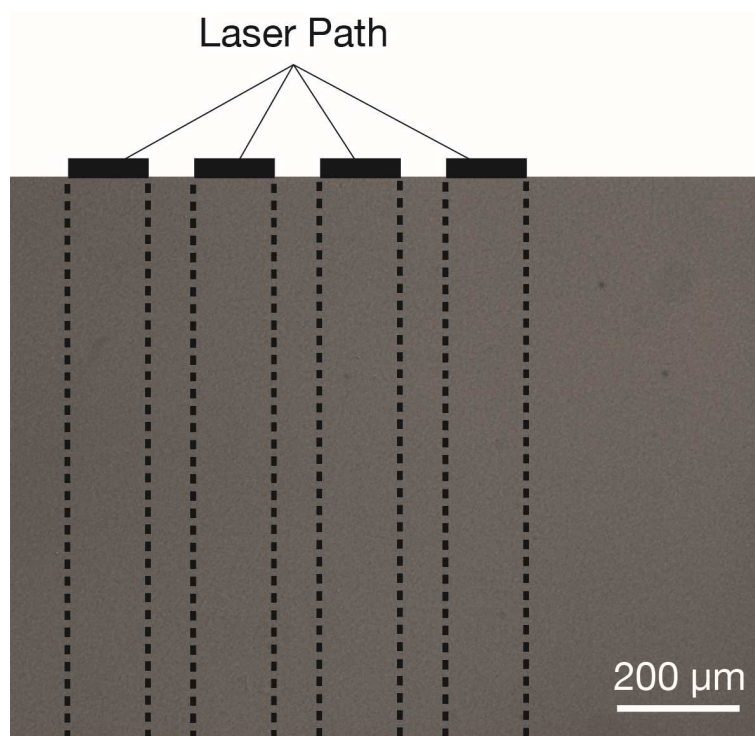
Supplementary Figure 4.5. Top view of a collagen hydrogel without nanorods showing no response to NIR light at maximum power and slow writing speeds (290 mW, 0.25 mm/s, respectively).
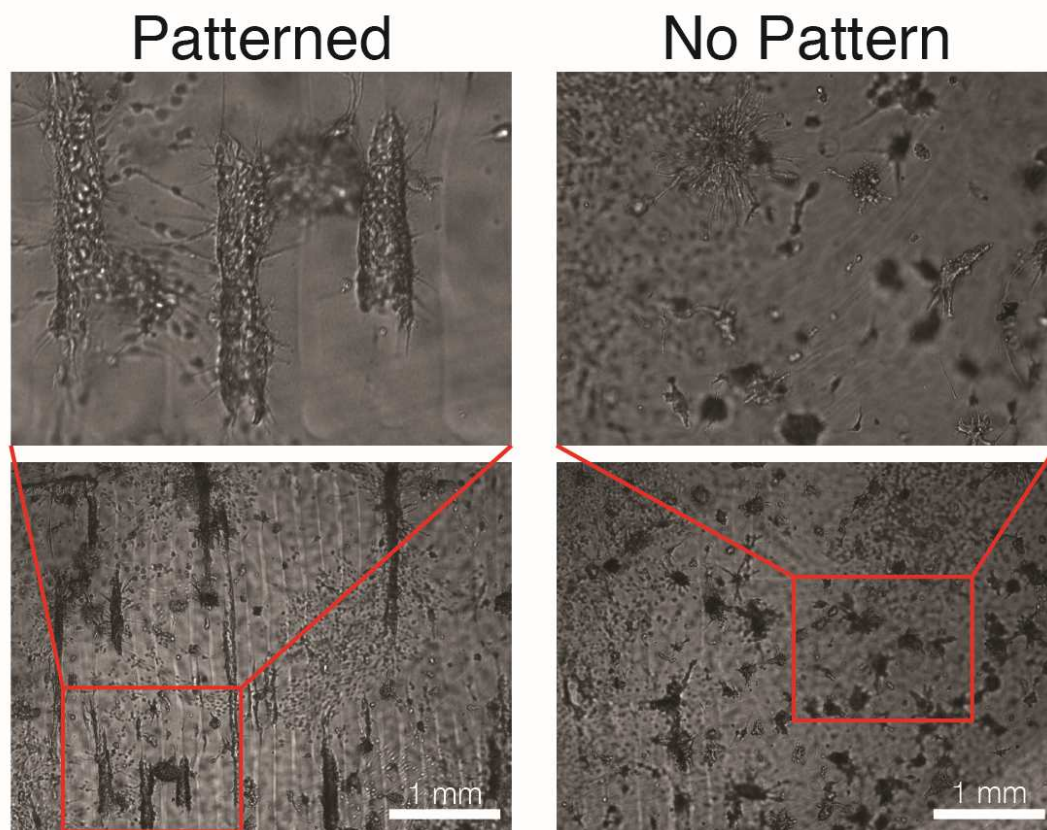
Supplementary Figure 4.6. Cell response to patterned and unpatterned collagen gels with gold nanorods after 14 days of culture.

## 4.6 References

1. Griffith, L. G.; Naughton, G., Tissue engineering - Current challenges and expanding opportunities. *Science* 2002, *295* (5557), 1009-+.

2. Bae, H.; Puranik, A. S.; Gauvin, R.; Edalat, F.; Carrillo-Conde, B.; Peppas, N. A.; Khademhosseini, A., Building vascular networks. *Science translational medicine* 2012, *4* (160), 160ps23.

3. Aizawa, Y.; Wylie, R.; Shoichet, M., Endothelial cell guidance in 3D patterned scaffolds. *Advanced materials* 2010, *22* (43), 4831-5.

4. Aubin, H.; Nichol, J. W.; Hutson, C. B.; Bae, H.; Sieminski, A. L.; Cropek, D. M.; Akhyari, P.; Khademhosseini, A., Directed 3D cell alignment and elongation in microengineered hydrogels. *Biomaterials* 2010, *31* (27), 6941-6951.

5. Cukierman, E.; Pankov, R.; Yamada, K. M., Cell interactions with three-dimensional matrices. *Current opinion in cell biology* 2002, *14* (5), 633-9.

6. Loessner, D.; Stok, K. S.; Lutolf, M. P.; Hutmacher, D. W.; Clements, J. A.; Rizzi, S. C., Bioengineered 3D platform to explore cell-ECM interactions and drug resistance of epithelial ovarian cancer cells. *Biomaterials* 2010, *31* (32), 8494-506.

7. Rouwkema, J.; Rivron, N. C.; van Blitterswijk, C. A., Vascularization in tissue engineering. *Trends in biotechnology* 2008, *26* (8), 434-41.

8. Novosel, E. C.; Kleinhans, C.; Kluger, P. J., Vascularization is the key challenge in tissue engineering. *Advanced drug delivery reviews* 2011, *63* (4-5), 300-11.

9. Brandl, F.; Sommer, F.; Goepferich, A., Rational design of hydrogels for tissue engineering: impact of physical factors on cell behavior. *Biomaterials* 2007, *28* (2), 134-46.

10. Hribar, K. C.; Soman, P.; Warner, J.; Chung, P.; Chen, S., Light-assisted direct-write of 3D functional biomaterials. *Lab on a chip* 2014, *14* (2), 268-75.

11. Zhang, A. P.; Qu, X.; Soman, P.; Hribar, K. C.; Lee, J. W.; Chen, S.; He, S., Rapid fabrication of complex 3D extracellular microenvironments by dynamic optical projection stereolithography. *Advanced materials* 2012, *24* (31), 4266-70.

12. Kolesky, D. B.; Truby, R. L.; Gladman, A. S.; Busbee, T. A.; Homan, K. A.; Lewis, J. A., 3D bioprinting of vascularized, heterogeneous cell-laden tissue constructs. *Advanced materials* 2014, *26* (19), 3124-30.

13. DeForest, C. A.; Anseth, K. S., Cytocompatible click-based hydrogels with dynamically tunable properties through orthogonal photoconjugation and photocleavage reactions. *Nature chemistry* 2011, *3* (12), 925-31.

14. Kloxin, A. M.; Kasko, A. M.; Salinas, C. N.; Anseth, K. S., Photodegradable hydrogels for dynamic tuning of physical and chemical properties. *Science* 2009, *324* (5923), 59-63.

15. Hribar, K. C.; Lee, M. H.; Lee, D.; Burdick, J. A., Enhanced release of small molecules from near-infrared light responsive polymer-nanorod composites. *ACS nano* 2011, *5* (4), 2948-56.

16. Hribar, K. C.; Choi, Y. S.; Ondeck, M. G.; Engler, A. J.; Chen, S., Digital Plasmonic Patterning for Localized Tuning of Hydrogel Stiffness. *Adv Funct Mater* 2014, *24* (31), 4922-4926.

17. Weissleder, R., A clearer vision for in vivo imaging. *Nature biotechnology* 2001, *19* (4), 316-7.

18. Bozec, L.; Odlyha, M., Thermal denaturation studies of collagen by microthermal analysis and atomic force microscopy. *Biophysical journal* 2011, *101* (1), 228-36.

19. Miller, J. S.; Stevens, K. R.; Yang, M. T.; Baker, B. M.; Nguyen, D. H.; Cohen, D. M.; Toro, E.; Chen, A. A.; Galie, P. A.; Yu, X.; Chaturvedi, R.; Bhatia, S. N.; Chen, C. S., Rapid casting of patterned vascular networks for perfusable engineered three-dimensional tissues. *Nature materials* 2012, *11* (9), 768-74.

20. Baranski, J. D.; Chaturvedi, R. R.; Stevens, K. R.; Eyckmans, J.; Carvalho, B.; Solorzano, R. D.; Yang, M. T.; Miller, J. S.; Bhatia, S. N.; Chen, C. S., Geometric control of vascular networks to enhance engineered tissue integration and function. *Proceedings of the National Academy of Sciences of the United States of America* 2013, *110* (19), 7586-91.

21. Liao, H. W.; Hafner, J. H., Gold nanorod bioconjugates. *Chem Mater* 2005, *17* (18), 4636-4641.

# Chapter Five: Biomimetic Trichome Microstructures

## 5.1 Introduction

"Biomimetics" was first coined by Otto Schmitt in the 1950's to describe the study of natural processes and mechanisms for the purpose of gaining inspiration for new human technologies. This idea was not novel, but Schmitt was able to bring the idea to the forefront of research minds just as he founded the field of biomedical engineering. The argument for using nature as inspiration is not a hard one to follow; why wouldn't we use millions of years of evolution as validation or inspiration for new ideas? There are numerous biomimetic technologies have been successfully developed and integrated into society. Examples include: Velcro, inspired by the hooked seeds of a burdock plant; self-cleaning surfaces, inspired by the surfaces of lotus plants; dry adhesive tape, inspired by gecko feet; and drag reducing edges, inspired by the ridges on shark skin.[1] These examples are well known and offer prime example of how biological structures can inspire innovative new technologies. While replicating nature is an exciting process, improving the designs offered by nature is even more exciting. In this chapter I will detail how a precise fabrication tool such a femtosecond laser can be used to replicate biological structures and more interestingly; improve them.

## 5.2 Bed Bugs and Bean Leaves

In recent years, societies across the world have seen a resurgence of the common bed bug *Cimex lectularius L.* The resurgence comes as the bed bug recovers from near eradication due to synthetic pesticides. Now, bed bugs are returning with an evolved resistance to chemical repellants.[2] There is no single cause of this resurgence but likely it is due to a variety of factors such as greater international commerce and travel, increased exchange of second hand furniture, and lack of knowledge of the pest. The resurgence has led to an unprecedented demand for research on its biology as outbreaks spread across the world.[3]

As the common bed bug spreads to new parts and more parts of the world, the demand for a remedy increases. Bed bugs currently affect poorer people who cannot afford to routinely wash their sheets or buy new sheets when they find they have bed bugs. There currently exists no low cost method for eliminating bed bugs.[4] Interestingly, in Balkan countries, people used bean leaves to entrap bed bugs and subsequently burned the leaves. In response to this resurgence, a group at UC Irvine investigated the mechanism of bean leaf entrapment and discovered the surface of the bean leaves was covered in tiny micro-hooks or trichomes which could impale or entrap the bed bugs.[5] They observed that, while both the bean leaf and bed bug evolved independently, the trichomes were able to pierce the bed bug's legs and entrap the bugs. This corroborated the results of Richardson who originally investigated the bean leaf-bed bug trapping phenomenon in 1943[6]. They found that 90% of the bed bugs were entrapped via piercing after 19 locomotory cycles, where a locomotory cycle refers to a single step be each of the six legs. This translates to mere seconds after placement of leaf. After the bugs were

trapped by one trichome they struggled to get free and further entrapped themselves by piercing other legs. Due to this effectiveness the group attempted to replicate the surface of the leaf and successfully did so while retaining trichome tip sharpness and density. The group used a two mold step process to replicate the surface of bean leaves which contained these microscopic trichomes. They first created a negative mold of the actual leaf and then made a positive mold, filling in the trichomes over the negative mold to create synthetic trichomes. They found however, that no bugs were successfully entrapped by their synthetic trichomes and concluded that the bending or twisting behavior of the trichome stalks is an integral part of the piercing process and their material and geometric design choice limited their success. They observed that the stalks of the natural trichomes were hollow and the tips were solid while their synthetic stalks were solid which may have made the flexural and torsional stiffness greater in the solid trichomes. They speculated that the more flexible natural trichomes could have 'skitter[ed] along the cuticle of the bug's surface until the shark point ended up in a crevice or pit…while a stiffer solid synthetic trichome may simply bend away.'

## 5.3 Rational Design

The femtosecond laser system allowed for precise manufacturing of trichomes (Figure 5.1) with tips very similar to the tips of the natural trichomes (Figure 5.1D). However the significance of rational design lies not in the ability to replicate nature, but to improve upon the design of nature and change the design to suit our application. We can create arrays of trichomes with much higher density and trichomes with multiple tips.

If the proportion of trapped bed bugs indeed is dependent on the trichome density which the group found to be 106 trichomes per mm$^2$, we can create dense arrays of trichomes limited only by physical space, thus increasing the effectiveness of the entrapment. Additionally the tips of trichomes can be designed to have multiple points which would allow for a higher probably of snaring or impaling the leg of a bug.

## 5.4 Fabrication of Trichomes

The same mechanism of two-photon polymerization was used to fabricate the trichomes as described in detail in Chapter 2.1.2. Instead of being limited to biocompatible polymers as in Chapter Three, we were able to use dipentaerythritol pentaacrylate (DPPA, Sartomer Inc., Exton, PA) for ease of fabrication. DPPA is preferred because it is fast curing due to the five acrylate groups in each of its molecules and it has strong abrasion resistance and flexibility with hardness that makes it very suitable for molds. In order to increase the TPP rate of DPPA, 1% photoinitiator (Irgacure 819, Ciba Specialty Chemicals, Tarrytown, NY) was mixed with DPPA at 80 degrees C. DPPA is also an ideal polymer because, when a photopolymer absorbs two photons simultaneously, it is equivalent to absorbing a single photon at half the wavelength. Therefore DPPA's high absorption at 400nm and negligible absorption at 800nm makes it ideal.[6] The trichomes were fabricated on the side of slab created by the DMD described in Chapter 2. The slab of DPPA provided an anchor for the trichome fabrication and will allow for ease of molding (Figure 5.1A).

## 5.5 Conclusion

While in its early stages, this project has a great deal of potential. SEM images shown in Figure 5.1 show the femtosecond laser is capable of making the structures with necessary precision. The next steps are to create an array and use a similar two step mold process to create a large enough array to interact with the bed bugs. Once the design of the trichomes can be validated by permanent entrapment via piercing the tarsi of the bugs, then much larger arrays can be fabricated to create surfaces which can effectively trap the bugs.
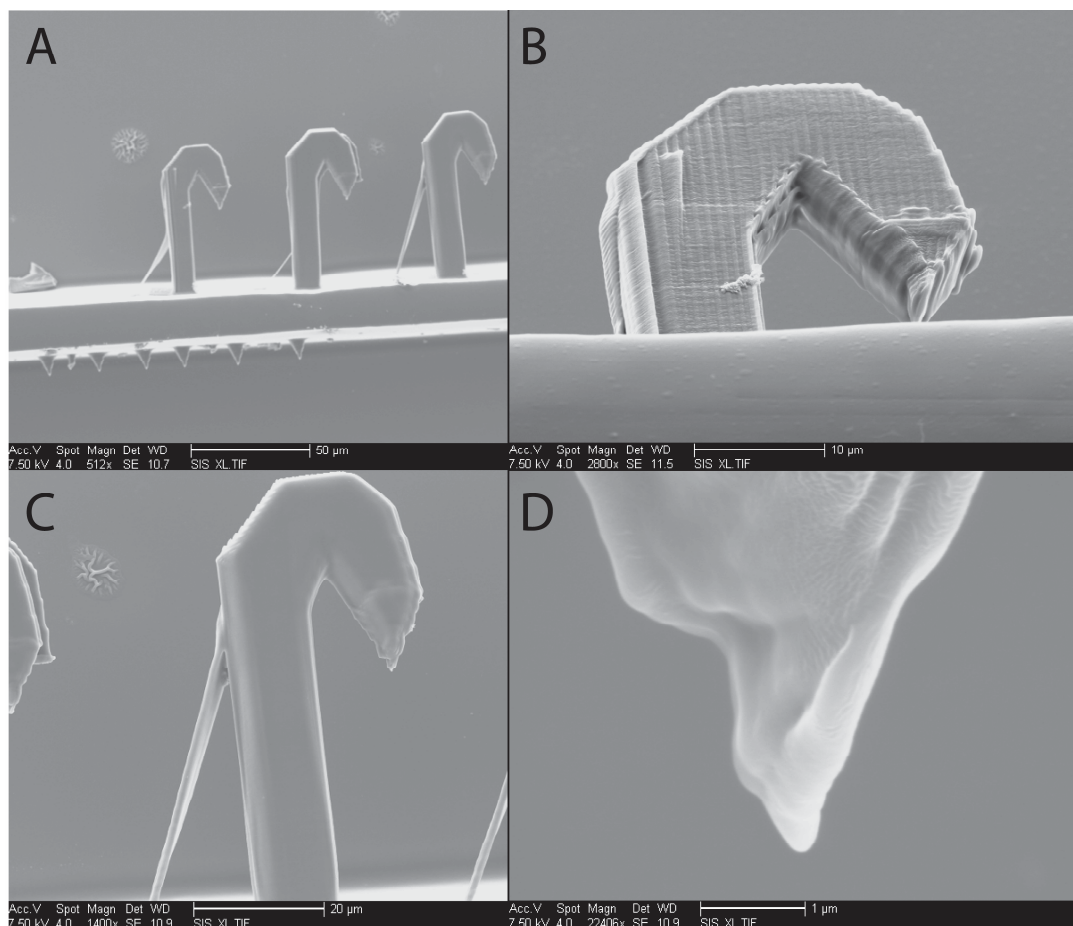
Figure 5.1. SEM images of trichomes fabricated with the femtosecond laser system using the material DPPA. Figure A shows an array of trichomes and demonstrates the capability to fabricate arrays much more dense then those naturally occurring on a bean leave. Figure 5.1B shows a tilted view a trichome fabricated with low power at 20mW. In contrast to Figure 5.1C, 5.1B's lower power results in texture on the surface as the width of each line barely overlaps with the nearest next line. Figure 5.1C shows a standalone trichome fabricated at 40mW. The surface is much smoother and the thickness of each line allows for a complete overlap. Figure 5.1D shows the tip of the trichome. The scale bar is 1um and the tip was calculated to be less than 400nm using ImageJ.

## 5.6 References

1.  Vincent, Julian F V, Olga A Bogatyreva, Nikolaj R Bogatyrev, Adrian Bowyer, and Anja-Karina Pahl. 2006. "Biomimetics: Its Practice and Theory." *Journal of the Royal Society, Interface / the Royal Society* 3 (9): 471–82. doi:10.1098/rsif.2006.0127.

2.  Johnson, E. R., & Goldstein, J. (2015). Biomimetic Futures: Life, Death, and the Enclosure of a More-Than-Human Intellect. Retrieved from http://www.tandfonline.com/doi/full/10.1080/00045608.2014.985625#.VVyx2_1VhuA

3.  Saenz, Virna L., Warren Booth, Coby Schal, and Edward L. Vargo. 2012. "Genetic Analysis of Bed Bug Populations Reveals Small Propagule Size Within Individual Infestations but High Genetic Diversity Across Infestations From the Eastern United States." *Journal of Medical Entomology* 49 (4). The Oxford University Press: 865–75. doi:10.1603/ME11202.

4.  Koganemaru, R., & Miller, D. M. (2013). The bed bug problem: Past, present, and future control methods. *Pesticide Biochemistry and Physiology*, *106*(3), 177–189. http://doi.org/10.1016/j.pestbp.2013.05.00

5.  Richardson, H. H. 1943. "The Action of Bean Leaves Against the Bedbug." *Journal of Economic Entomology* 36 (4). The Oxford University Press: 543–45. doi:10.1093/jee/36.4.543.

6.  Zhang, W. (2012). *Investigation of cell environment interaction in vitro using a femtosecond laser* (Order No. 3540363). Available from Dissertations & Theses @ University of California; ProQuest Dissertations & Theses A&I. (1112486292). Retrieved from http://search.proquest.com/docview/1112486292?accountid=14524